Available online at www.sciencedirect.com
ScienceDirect
Journal of Sound and Vibration 309 (2008) 637–676
JOURNAL OF SOUND AND VIBRATION
www.elsevier.com/locate/jsvi

Nonlinear stability of cylindrical shells subjected to axial flow: Theory and experiments

K.N. Karagiozis[a], M.P. Païdoussis[a,*], M. Amabili[b], A.K. Misra[a]

[a]*Department of Mechanical Engineering, McGill University, 817 Sherbrooke Street West, Montreal, Québec, Canada H3A 2K6*
[b]*Dipartimento di Ingegneria Industriale, Università di Parma, Parco Area delle Scienze 181/A, Parma I-43100, Italy*

Received 22 February 2006; received in revised form 8 March 2007; accepted 24 July 2007
Available online 23 October 2007

Abstract

This paper, is concerned with the nonlinear dynamics and stability of thin circular cylindrical shells clamped at both ends and subjected to axial fluid flow. In particular, it describes the development of a nonlinear theoretical model and presents theoretical results displaying the nonlinear behaviour of the clamped shell subjected to flowing fluid. The theoretical model employs the Donnell nonlinear shallow shell equations to describe the geometrically nonlinear structure. The clamped beam eigenfunctions are used to describe the axial variations of the shell deformation, automatically satisfying the boundary conditions and the circumferential continuity condition exactly. The fluid is assumed to be incompressible and inviscid, and the fluid–structure interaction is described by linear potential flow theory. The partial differential equation of motion is discretized using the Galerkin method and the final set of ordinary differential equations are integrated numerically using a pseudo-arclength continuation and collocation techniques and the Gear backward differentiation formula. A theoretical model for shells with simply supported ends is presented as well. Experiments are also described for (i) elastomer shells subjected to annular (external) air-flow and (ii) aluminium and plastic shells with internal water flow. The experimental results along with the theoretical ones indicate loss of stability by divergence with a subcritical nonlinear behaviour. Finally, theory and experiments are compared, showing good qualitative and reasonable quantitative agreement.

1. Introduction

Thin-walled circular cylindrical shell structures containing or immersed in flowing fluid may be found in many engineering and biomechanical systems. Most of the studies on the aeroelasticity of cylindrical shells are for compressible and particularly supersonic flows, reflecting the enormous interest on the effects of high-speed flow on the outer-skin panels of aircraft, missiles and aerospace vehicles [1]. However, there are many other applications in which shells are subjected to incompressible or subsonic flows that are also of great interest [2]; for example: thin cylindrical shells used as thermal shields in nuclear reactors and heat shields in aircraft engines; shell structures in jet pumps, heat exchangers and storage tanks; thin-walled piping for

*Corresponding author.
E-mail address: mary.fiorilli@mcgill.ca (M.P. Païdoussis).

0022-460X/$ - see front matter © 2007 Elsevier Ltd. All rights reserved.
doi:10.1016/j.jsv.2007.07.061

aerospace vehicles; and in the construction of shell-type Coriolis mass-flow meters. Furthermore, in biomechanics, veins, pulmonary passages and urinary systems can be modelled as shells conveying fluid.

For a long time, it was believed that subsonic/incompressible flows were associated with loss of stability in the form of mild (small amplitude) divergence—in contrast to the flutter and richer dynamics observed with supersonic flows. Nevertheless, the work of Païdoussis and Denise [3] sparked new interest in the analysis of thin shells subjected to subsonic flows. They provided the first linear analytical model for clamped–clamped shells, i.e., shells with both ends clamped, and clamped–free shells conveying inviscid fluid, along with experimental results. The analytical model is based on Flügge's shell equations and potential flow theory; the equations are solved using a travelling-wave solution. The experimental results, for shells with clamped ends, showed that at sufficiently high flow velocity the system develops flutter, with shell amplitudes much larger than the shell thickness. In contrast, the theoretical model predicts that the system loses stability by divergence, and then at higher flow velocity by coupled-mode flutter. The predicted coupled-mode flutter originates directly from a divergent state, i.e., without restabilization in-between; this is known in the literature as "Païdoussis coupled-mode flutter" [4]. The interval between divergence and flutter is small, especially if the fluid conveyed is air. Hence, in the Païdoussis and Denise experiments, it was reasoned that flutter was entrained by the divergence, and that was the reason why divergence by itself was not observed. In the case of annular (external) flow, however, divergence was observed but not flutter, as reported by El Chebair et al. [5]—though the maximum flow velocities available were probably insufficient for deciding unequivocally that flutter does not exist at higher flows.

Both theoretical results and experimental observations are perplexing insofar as the dynamics of clamped–clamped shells with internal flow is concerned [6]. The system is inherently conservative and so ought to lose stability by divergence, not flutter. Also, the very existence of flutter is problematic, since it has been shown theoretically that the work done in a putative cycle of oscillation is zero. In this regard, it is to be noted that in the Païdoussis and Denise experiments the flutter amplitudes were large: measured in fractions of the radius rather than of the thickness. It is known that large radial shell deformations, of the order of the shell thickness, may result in important nonlinear effects. Hence, mindful of the controversy on the existence of post-divergence coupled-mode flutter in pipes with supported ends conveying fluid, which was only resolved via nonlinear theory (see Refs. [2,7,8]), it is obvious that its existence for the shell problem would have to be decided by nonlinear theory in this case also—thereby possibly also clarifying the non-existence of divergence in the internal flow experiments.

In the Païdoussis and Denise [3] investigation for cantilevered shells with internal flow, however, both experimental and linear theoretical results indicate that the shell loses stability by flutter.

There is a significant numbers of other linear studies on shells subjected to internal or external incompressible or subsonic flow, by Weaver and Unny [9], Weaver and Myklatun [10], Shayo and Ellen [11], and many others.

Some work also exists on the dynamics of coaxial shells with internal and/or annular fluid flow. Païdoussis et al. [12] developed an analytical model to study the dynamics and stability of coaxial cylindrical shells conveying incompressible or compressible fluid in the inner and annular space between the two shells, using Flügge's linear shell theory and potential flow for the fluid–structure interaction. They employed a Fourier transform technique for the solution of the problem. It was found that the annular flow destabilizes the system at lower flow velocities than flow in the inner shell and that the stability threshold is lower when both shells are flexible. The effect of compressibility was found to be small. Subsequently, Païdoussis et al. [13] studied the dynamics and stability of coaxial cylindrical shells conveying *viscous fluid*. It was found that the effect of viscosity in the annular region tends to destabilize the system, *vis-à-vis* inviscid flow, whereas viscous effects in the inner flow stabilize the system.

El Chebair et al. [5] performed an experimental study on the dynamical behaviour of a cylindrical shell with clamped ends within a coaxial rigid cylindrical pipe, with flow in the annular region. It was found that the shell loses stability by divergence (buckling). The theoretical model developed was in good qualitative and reasonable quantitative agreement with the experimental results. El Chebair et al. [14] extended the model to include the effect of unsteady viscous forces on internal and annular-flow-induced instabilities of the system. It was found that the unsteady viscous forces can be neglected for fairly large annular gaps; in contrast, for smaller annular gaps these effects are more pronounced, rendering the system more stable. When both steady

and unsteady viscous forces are considered in the annular flow case, the system loses stability at much lower velocities for all annular gaps, because of the predominance of the steady viscous effects.

Païdoussis et al. [15] studied the stability of clamped–free coaxial shells conveying incompressible fluid in the annular space in-between and within the inner shell, taking steady viscous effects into account, but neglecting the unsteady ones. They used Flügge's linear shell equations and potential flow theory to model the fluid–structure interaction, and solved the equations of motion by the Fourier transform method. Different outflow models were used to satisfy the downstream fluid boundary conditions. They concluded that the shell loses stability by flutter for internal flow, according to both inviscid and viscous flow models; interestingly, for the annular flow, whereas the inviscid theory predicted loss of stability by flutter, viscous theory predicted loss of stability by divergence and then at appreciably higher flow by flutter. Nguyen et al. [16] conducted an experimental study on the stability of cantilevered coaxial cylindrical shells conveying fluid. The shell was found to lose stability by flutter. A CFD-based model, developed by Nguyen et al. [17], examined the stability of cantilevered coaxial shells conveying viscous fluid. The model was in excellent quantitative agreement with experiments, although there was a small discrepancy in predicting the correct type of instability (divergence or flutter) in some cases.

The nonlinear studies available for shells in contact with flowing fluid are few. Most of the early studies were motivated by the enormous interest in missile applications, thus involving high-speed, compressible and often supersonic flows. Examples of this class of studies are: Stearman et al. [18], Olson and Fung [19], Evensen and Olson [20], Barr and Stearman [21], Horn et al. [22], Librescu [23], Vol'mir [24,25] and Dowell [1].

Païdoussis [2] presented a set of very extensive but unpublished experiments conducted by Guernier [26] on cantilevered elastomer shells with low-speed internal air-flow. The shell lost stability by flutter. The critical flow velocity for the onset of flutter was influenced by flow perturbations, resulting in critical flow velocities as much as three times lower than for undisturbed flow. It was concluded that the dynamical behaviour showed a strong hysteresis in the onset and cessation of self-excited flutter, depending on the length-to-radius ratio.

The first theoretical studies on the nonlinear vibrations of shells with incompressible internal flow are attributed to Lakis and Laveau [27] and Selmane and Lakis [28]. Results showed that the fluid nonlinearities could be neglected in the analysis of free shell vibrations of physical amplitude. In the latter study the nonlinear structural model was coupled with the nonlinear fluid model, producing a more general model for open shells. It was found that the nonlinear response (softening or hardening) depends on the circumferential wavenumber of the vibration.

Amabili et al. [29–32] in a benchmark series of papers developed a nonlinear analytical model for simply supported shells conveying incompressible inviscid fluid using the Donnell nonlinear shallow shell theory and an adaptation of the Païdoussis and Denise [3] fluid–structure interaction model. Various variants of this analysis consider (i) different modal expansions, showing that axisymmetric modes are essential for capturing the dynamics properly, (ii) the contribution of the companion modes, etc. The most significant findings of this research are two: (a) the system loses stability by a strongly subcritical pitchfork bifurcation, which means that, given enough perturbation, divergence may occur at much lower flows than the linear threshold; and (b) only static solutions are found to exist beyond the first bifurcation, some stable and some unstable, but no oscillatory solutions. It must be pointed out that the work of Amabili et al. [31] succeeded in obtaining for the first time the full solution of the problem, even if only for simply supported boundary conditions, allowing the understanding of the physics of the phenomenon.

Further work on the same problem was conducted by Amabili et al. [33], specifically on (i) the stability of simply supported shells conveying incompressible fluid, using the Donnell nonlinear equations and additional degrees of freedom (dof) to study the convergence of the solution, and (ii) the response of the fluid-conveying shell to a harmonic point load. They used a seven dof modal expansion including driven and companion modes along with axisymmetric modes, thus allowing for circumferential travelling wave solutions; they also explored the effect of higher-order expansions, up to 18 dof. In the absence of the harmonic load the shell lost stability by divergence, experiencing softening-type nonlinearity. Under harmonic load excitation the fluid-conveying shell was subject to periodic, quasi-periodic and chaotic responses, depending on flow velocity, amplitude and frequency of the harmonic excitation.

The nonlinear stability of circular cylindrical shells in annular and unbounded axial compressible (subsonic) flow was considered in the work of Amabili et al. [34]. They used the nonlinear Donnell shallow shell theory

for simply supported shells for two cases: (i) with zero axial force at the shell edges; and (ii) with zero axial displacement at the two ends of the shell. The fluid–structure interaction was modelled using linear potential flow theory. Results for both annular and unbounded external flow showed that the system loses stability by divergence through strongly subcritical bifurcations.

Amabili and Pellicano [35] studied the stability of simply supported circular cylindrical shells in supersonic flow via Donnell's nonlinear shallow shell theory and linear piston theory. The system was found to lose stability by flutter travelling around the shell, through a supercritical bifurcation. The theoretical results are in good agreement with existing experimental data. Amabili and Pellicano [36] extended their model to a 22-mode expansion and extended the linear piston theory to third-order. They also considered geometric imperfections of the shell. Numerical calculations for Mach number $M = 3$ were successfully compared for the first time with results obtained more than 30 years before at the NASA Ames Research Center. The system was found to lose stability by travelling wave flutter through a supercritical bifurcation. The theoretical results are in good agreement with experiments for the onset of flutter, the flutter amplitude, and the frequency. They also concluded that the effects of shell imperfections are important. It was shown that the difference between linear and nonlinear piston theory is negligible.

The only literature available on the nonlinear dynamics and stability of circular cylindrical shells with *clamped ends* subjected to internal or annular incompressible flow is the work of Karagiozis [37], Karagiozis et al. [38–40] and Karagiozis et al. [41]. Refs. [37–40] examined the nonlinear behaviour of clamped shells subjected to axial fluid flow experimentally. The shells lost stability by divergence via a strongly subcritical pitchfork bifurcation; thus, there was a large hysteresis involved. In addition, the phenomenon of oscillatory (''dynamic'') divergence was captured experimentally for clamped elastomer shells with internal air-flow. Refs. [37–39] are conference presentations and a thesis, while Ref. [41] deals with the theory for empty and fluid-filled shells but with the fluid not flowing. Additional work on the nonlinear vibration of clamped shells excited by an external excitation is presented by Amabili [45]; in this work a combination of sine and cosine functions was used describing successfully the u, v and w displacements of the clamped shell. Consequently, the present paper is the first archival presentation of the nonlinear theoretical model for shells with clamped ends containing flowing fluid.

The following sections of this paper present and discuss the theoretical development of the nonlinear model for clamped–clamped shells in contact with flowing fluid in detail. For completeness, the model for simply supported shells is also presented, and it is used in Section 5 of this study. Theoretical results obtained from the model described in Section 2 are presented in Section 3 of the paper. In Section 4, the experiments conducted to validate the theory are discussed, and a new set of experimental results is presented for shells with internal or external fluid flow. A comparison between theoretical and experimental results is presented in Section 5 of this paper.

2. Theoretical development

The construction of two different theoretical models for shells subjected to axial fluid flow is presented in this section. Model CC is specifically developed in the present study to deal with shells with fully clamped extremities. Model SS was originally developed by Amabili et al. [29] for cylindrical shells with classical simply supported ends; it is employed in generating theoretical results used for comparison with some of the experiments in Section 5.

2.1. Formulation of the structural nonlinear model

Fig. 1 shows the system under consideration. It consists of a thin, closed circular cylindrical shell of length L, mean radius R, and thickness h. A cylindrical coordinate system is chosen as shown in Fig. 1. The shell is assumed to be of homogeneous, isotropic elastic material of Young's modulus E and Poisson ratio ν.

The coordinate system is taken along the middle surface of the shell, with u, v and w being the displacement components in the axial, circumferential and radial direction, respectively.

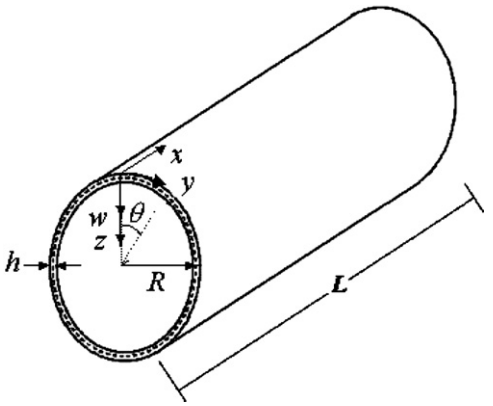

Fig. 1. Shell geometry and coordinate system used for clamped–clamped and simply supported shells.

Assuming a positive radial deformation w inwards, as in Fig. 1, the simplified Donnell nonlinear shallow-shell equation is

$$D\nabla^4 w + ch\dot{w} + \rho h\ddot{w} = f - p + \frac{1}{R}\frac{\partial^2 F}{\partial x^2} + \left(\frac{\partial^2 F}{\partial y^2}\frac{\partial^2 w}{\partial x^2} - 2\frac{\partial^2 F}{\partial x \partial y}\frac{\partial^2 w}{\partial x \partial y} + \frac{\partial^2 F}{\partial x^2}\frac{\partial^2 w}{\partial y^2}\right), \tag{1}$$

where F is the in-plane Airy stress function satisfying the following compatibility equation:

$$\frac{1}{Eh}\nabla^4 F = -\frac{1}{R}\frac{\partial^2 w}{\partial x^2} - \frac{\partial^2 w}{\partial x^2}\frac{\partial^2 w}{\partial y^2} + \left(\frac{\partial^2 w}{\partial x \partial y}\right)^2; \tag{2}$$

$D = Eh^3/[12(1-\nu^2)]$ is the flexural stiffness of the shell, c (kg/m^3 s) the structural damping coefficient, and ρ the mass density of the shell; f represents the summation of all external forces acting on the surface per unit area of the shell in the radial direction, set equal to zero in the present study, and p the transmural pressure acting on the surface of the shell. The biharmonic operator is defined as $\nabla^4 = [\partial^2(\ )/\partial x^2 + \partial^2(\ )/\partial y^2]^2$, and the overdots represent time derivatives. Eqs. (1) and (2) correspond to the *shallow shell* approximation, and accordingly apply for shell deformations dominated by the radial displacement w; in fact, in-plane inertia is neglected. For cylindrical shells, shallow shell theory applies if the number of circumferential waves, n, is such that $1/n^2 \ll 1$; i.e., the minimum number of nodal diameters should be at least $n = 4$ or 5 [42].

The expressions for the stress resultants per unit length in the axial and circumferential directions along with the shear stress resultant are given by

$$N_x = \frac{\partial^2 F}{\partial y^2}, \quad N_y = \frac{\partial^2 F}{\partial x^2}, \quad N_{xy} = -\frac{\partial^2 F}{\partial x \partial y}, \tag{3}$$

and the strain–displacement relations are related to the shell displacements by

$$(1-\nu^2)\frac{N_x}{Eh} = -\frac{\nu w}{R} + \frac{1}{2}\left(\frac{\partial w}{\partial x}\right)^2 + \frac{\nu}{2}\left(\frac{\partial w}{\partial y}\right)^2 + \frac{\partial u}{\partial x} + \nu\frac{\partial v}{\partial y}, \tag{4a}$$

$$(1-\nu^2)\frac{N_y}{Eh} = -\frac{w}{R} + \frac{\nu}{2}\left(\frac{\partial w}{\partial x}\right)^2 + \frac{1}{2}\left(\frac{\partial w}{\partial y}\right)^2 + \nu\frac{\partial u}{\partial x} + \frac{\partial v}{\partial y}, \tag{4b}$$

$$(1-\nu^2)\frac{N_{xy}}{Eh} = 2(1-\nu)\left[\frac{\partial w}{\partial x}\frac{\partial w}{\partial y} + \frac{\partial u}{\partial y} + \frac{\partial v}{\partial x}\right]. \tag{4c}$$

Two different sets of boundary conditions are employed. In the development of the CC model the general form of the boundary conditions is

$$u = v = w = 0 \quad \text{and} \quad \partial w/\partial x = 0 \ \text{ at } \ x = 0 \quad \text{and} \quad x = L. \tag{5a}$$

In the case of the SS model the classical simply supported boundary conditions are

$$v = w = 0,\ N_x = 0 \quad \text{and} \quad M_x = -D\{(\partial^2 w/\partial x^2) + v(\partial^2 w/\partial y^2)\} = 0 \text{ at } x = 0 \quad \text{and} \quad x = L. \tag{5b}$$

In the foregoing formulation, the displacements u and v have been eliminated and only w is considered in the equation of motion. However, both u and v appear in the strain–displacement expressions given in Eqs. (4). The axial constraints imposed by the boundary conditions at the two ends of the shell must be satisfied exactly by the solution expansion of the radial deformation $w(x, y, t)$. In addition to the essential boundary conditions, each model must satisfy the condition of circumferential continuity in v.

2.2. Solution expansion

In order to reduce the continuous system to one of finite dimension, i.e., to discretize the system, the displacement w is expanded using an appropriate set of basis (shape) functions. The choice of the shape functions has been a topic of wide discussion in the literature. The selection of the type of shape functions used in the solution expansion may alter the outcome of the nonlinear response of a shell subjected to a mechanical or flow-related load.

There are few studies for clamped–clamped shells in the literature that discuss the choice of the shape functions in the solution expansion. One such suggestion was made by Matsuzaki and Kobayashi [43] for an expansion involving the driven and companion modes and a cosine-squared axisymmetric term. Another expansion is recommended by Yamaki [44], but it does not satisfy the requirement of continuity in the circumferential direction.

In the work of Amabili et al. [29] for simply supported shells, it was suggested that the best choice of appropriate shape functions is offered by the use of the eigenfunctions of the corresponding linear problem. The beam eigenfunctions offer two major advantages: (i) they satisfy the essential boundary conditions exactly; (ii) they are orthogonal. Moreover, in the solution expansion it is necessary to consider, along with the asymmetric mode directly driven into vibration by the excitation (the so-called *driven mode*), (i) the orthogonal mode having the same shape and natural frequency but rotated by $\pi/(2n)$ (the *companion mode*), (ii) additional asymmetric (both driven and companion) modes, and (iii) axisymmetric modes. It has firmly been established that, for large-amplitude shell vibrations, the deformation of the shell involves significant axisymmetric deformation inwards.

The proposed solution expansion used here for the CC model, i.e., for a clamped–clamped shell, is

$$w(x, y, t) = \sum_{m=1}^{M}\sum_{n=1}^{N}[A_{m,n}(t)\cos(ny/R) + B_{m,n}(t)\sin(ny/R)]\varphi_m(x) + \sum_{m=1}^{K} A_{2m-1,0}(t)\varphi_{2m-1}(t), \tag{6}$$

where φ_m are the eigenfunctions for a clamped–clamped beam defined by

$$\varphi_m(x) = \cosh(\lambda_m x/L) - \cos(\lambda_m x/L) - a_m[\sinh(\lambda_m x/L) - \sin(\lambda_m x/l)], \tag{7}$$

λ_m being the corresponding dimensionless eigenvalues obtained from solving the characteristic equation $\cosh\lambda\cos\lambda = 1$; m is the axial wavenumber (equal to the number of half-waves along the shell), n the circumferential wavenumber and $a_m = [\cosh\lambda_m - \cos\lambda_m]/[\sinh\lambda_m - \sin\lambda_m]$. The amplitude functions, $A_{m,n}(t)$, $B_{m,n}(t)$ and $A_{2m-1,0}(t)$, are the unknown generalized coordinates (time functions).

The first term of the expansion in Eq. (6), i.e., the double summation, involves the interaction between the linear asymmetric circumferential modes of nodal diameter $n > 0$, and all of the corresponding linear radial axisymmetric modes of m half-waves; this term consists of the driven mode (the terms involving $\cos(ny/R)$) along with the companion mode (the terms involving $\sin(ny/R)$)[1]. The last term of the expansion involves all the axisymmetric radial modes, with $n = 0$; this term has been shown to be very important in the stability analysis of simply supported shells [29]; in this term, axisymmetric modes with even values of m are neglected, because they do not contribute to shell contraction (the even m contractions along the length of the shell cancel out, having a zero average radial deformation).

[1]The terms driven and companion modes should strictly be used only in the presence of external excitation, but they are used here, in an analogous way, to define two families of modes orthogonal in θ.

In the case of the SS model, the solution expansion originally used by Amabili et al. [29] is also adopted here:

$$w(x,y,t) = \sum_{m=1}^{M}\sum_{n=1}^{N}[A_{m,n}(t)\cos(ny/R) + B_{m,n}(t)\sin(ny/R)]\sin(m\pi x/L) + \sum_{m=1}^{K} A_{2m-1,0}(t)\sin((2m-1)\pi x/L). \tag{8}$$

The mode expansions given in Eqs. (6) and (8) satisfy exactly the corresponding clamped–clamped and simply supported boundary conditions involving w, Eqs. 5(a) and (b), respectively. Both expansions independently satisfy both the continuity of the circumferential displacement and the null in-plane displacement v at the shell ends; different conditions have to be satisfied for u or N_x in the axial direction for the CC and SS models. These conditions for the CC model are:

$$\int_0^{2\pi R}\frac{\partial v}{\partial y}\mathrm{d}y = [v(x,2\pi R) - v(x,0)] = 0, \tag{9}$$

$$\int_0^{2\pi R}\int_0^{L}\frac{\partial u}{\partial x}\mathrm{d}x\mathrm{d}y = 0, \quad \int_0^{2\pi R}\int_0^{L}\frac{\partial v}{\partial y}\mathrm{d}x\mathrm{d}y = 0; \tag{10,11}$$

Eq. (10) is replaced by $N_x = 0$ at $x = 0$, L for the SS model. The mode expansions, Eqs. (6) and (8), satisfy independently Eqs. (9)–(11) when using the strain-displacement relationships given in Eqs. (4) together with the expression for the Airy stress function given in Section 2.6.1.

In the CC model, the modal solution (6) is expanded to seven, eight and eleven dof[2]; these will henceforth be referred to as the seven, eight and eleven dof models. For simplicity, in this section of the paper, the seven dof model is used for the detailed construction of the model. The mode expansion, for the seven dof CC model, is

$$\begin{aligned} w(x,y,t) = {} & [A_{1,n}(t)\cos(ny/R) + B_{1,n}(t)\sin(ny/R)]\varphi_1(x) \\ & + [A_{2,n}(t)\cos(ny/R) + B_{2,n}(t)\sin(ny/R)]\varphi_2(x) \\ & + A_{1,0}(t)\varphi_1(x) + A_{3,0}(t)\varphi_3(x) + A_{5,0}(t)\varphi_5(x). \end{aligned} \tag{12}$$

Nevertheless, in Section 5 numerical results involving the eight and eleven dof models are compared with experimental results; these models, not detailed here for brevity, were constructed to study the effect of including additional asymmetric and axisymmetric modes in the solution expansion on stability and on the nonlinear response of the shell.

In the case of the SS model, Amabili et al. [33] have extensively investigated the effect of high-order models on the stability of the shell. In this work the SS model used is one of 18 dof and is given by [29]

$$w(x,y,t) = \sum_{m=1}^{6}[A_{m,n}(t)\cos(ny/R) + B_{m,n}(t)\sin(ny/R)]\sin(m\pi x/L) + \sum_{m=1}^{6} A_{(2m-1),0}(t)\sin[(2m-1)\pi x/L]. \tag{13}$$

2.3. Fluid–structure interaction

Let us consider the case when there is fluid–structure interaction, i.e., when the term p is not zero in the Donnell nonlinear shallow shell equations, in Eq. (1).

The shell is assumed to be in contact with inviscid fluid, flowing in the axial direction. Furthermore, it is assumed that the fluid is incompressible and isentropic and the flow is irrotational. Nonlinearities in the dynamic pressure and in the boundary conditions at the fluid–structure interface are neglected, because fluid

[2]Additional details on the development of the eight and eleven dof models along with results obtained from these two models may be found in Karagiozis [37]. However, some results with these higher-order models are presented in Section 5.

movements of the order of the shell thickness may be considered to be small; and hence a linear formulation is quite reasonable. Indeed, such nonlinear effects have been found to be negligible by Gonçalves and Batista [46]; this was confirmed by Lakis and Laveau [27] and Selmane and Lakis [28] for closed circular cylindrical shells in contact with inviscid incompressible fluid. In addition, pre-stress in the shell due to fluid weight (hydrostatic effect) is neglected. With these assumptions, the fluid–structure interaction can be described by potential flow theory.

The irrotational property of the flow implies the existence of a scalar potential function of the form $\Psi(x,\theta,r,t)$. The velocities may be obtained from

$$V = \nabla\Psi. \tag{14}$$

The internal or external (annular) flow can be considered to comprise a mean flow and an unsteady flow. The mean flow velocity is associated with the undisturbed flow velocity U in the x-direction, and the unsteady flow with a potential function $\Phi(x,\theta,r,t)$, which is associated with shell motions. Therefore, the potential Ψ can be expressed as

$$\Psi = Ux + \Phi. \tag{15}$$

The components of the flow in cylindrical coordinates are given by

$$V_x = U + \partial\Phi/\partial x, \quad V_\theta = (1/r)\partial\Phi/\partial\theta, \quad V_r = \partial\Phi/\partial r. \tag{16}$$

In addition, the perturbation potential Φ must satisfy the Laplace equation

$$\nabla^2\Phi = \frac{\partial^2\Phi}{\partial x^2} + \frac{\partial^2\Phi}{\partial r^2} + \frac{1}{r}\frac{\partial\Phi}{\partial r} + \frac{1}{r^2}\frac{\partial^2\Phi}{\partial\theta^2} = 0. \tag{17}$$

The total perturbed pressure P acting on the fluid–shell interface is defined as the combination of the mean pressure $\bar{P}$ and the perturbation pressure p, i.e.,

$$P = \bar{P} + p. \tag{18}$$

Using Bernoulli's equation for the perturbed flow, the velocity potential is related to the perturbation pressure by

$$\partial\Phi/\partial t + \frac{1}{2}V^2 + \frac{P}{\rho_F} = \frac{P_s}{\rho_F}, \tag{19}$$

where $V^2 = V_x^2 + V_\theta^2 + V_r^2$, P_s is the stagnation pressure and ρ_F the fluid density. For small flow perturbations, V^2 can be linearized via Eq. (16) to $V^2 \simeq U^2 + 2U(\partial\Phi/\partial x)$. Therefore, using Eqs. (18) and (19) and $\bar{P} + \frac{1}{2}U^2 = P_s$, the perturbation pressure is given by

$$p = -\rho_F(\partial\Phi/\partial t + U\partial\Phi/\partial x). \tag{20}$$

The fluid domain is a cylinder (a hollow cylinder in the case of annular flow) of infinite extent lying within a periodically supported shell of infinite length[3]. It is important to assume that the solution expansion w is a periodic function from 0 to $2L$ and that w and the flow field is defined for any $x \in (-\infty, +\infty)$; see Fig. 2(b). The requirement that w be periodic with period $2L$ is essential if axisymmetric modes are included in the solution expansion w. The reason is that the change in volume of the fluid, when axisymmetric modes of odd longitudinal wavenumber are used, cancels out in $2L$. This type of solution was mathematically developed by Païdoussis and Denise [3] and later elaborated by Amabili et al. [29]. The advantage of this kind of solution in the present context is that it allows for (i) the inclusion of axisymmetric modes in the expansion of w and (ii) the utilization of the separation of variables method to solve for the velocity potential. Therefore,

[3]If, instead of assuming the system to be part of a periodically supported larger system, a baffled system is considered (as in Fig. 2(a)), difficulties arise, associated with the kinetic energy becoming indefinitely large for the axisymmetric components in the mode expansion, since continuity must be imposed across the baffles.

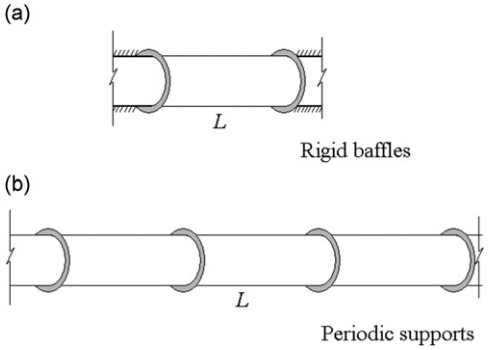

Fig. 2. Two different boundary conditions for clamped–clamped shells considered in the development of the fluid model: (a) system with rigid baffles at either end, extending to infinity; (b) the flexible shell as part of an infinite shell system with periodic supports.

the modal expansion in the solution must satisfy

$$w = w(x, y, t) \quad \text{for} \quad 0 \leqslant x \leqslant L,$$
$$w = -w(x - L, y, t) \quad \text{for} \quad L \leqslant x \leqslant 2L. \tag{21}$$

Consequently, there are no boundary conditions for the flow in the x-direction since the flow domain extends over $x \in (-\infty, +\infty)$. Nevertheless, the flow must satisfy the radial boundary conditions at the surface of the shell.

Assuming that no cavitation takes place, the impermeability condition at the shell boundary is given by $\mathrm{D}s(x, \theta, r, t)/\mathrm{d}t = 0$, where $\mathrm{D}(\ )/\mathrm{d}t$ is the substantial derivative. Setting $s = R - w(x, \theta, t)$, where s at any time is equal to the radius of the shell plus the instantaneous shell deformation, and substituting into the expression for the substantial derivative, we obtain

$$\mathrm{D}s/\mathrm{d}t = -(\partial w/\partial t + U\partial w/\partial x). \tag{22}$$

Therefore, the boundary conditions *for internal flow* are given by the following:

$$\text{the flow is finite} \quad \text{at} \quad r = 0,$$
$$V_r = \partial\Phi/\partial r = -(\partial w/\partial t + U\partial w/\partial x) \quad \text{at} \quad r = R_i, \tag{23}$$

where the second one is the impermeability condition and $R_i = R - h/2$. The radial boundary conditions *for annular flow* are given by

$$\partial\Phi/\partial r = 0 \quad \text{at} \quad r = r_i,$$
$$\partial\Phi/\partial r = -(\partial w/\partial t + U\partial w/\partial x) \quad \text{at} \quad r = R_o, \tag{24a, b}$$

where $R_o = R + h/2$, and r_i is the external radius of the fluid domain (see Fig. 3(b)).

The mode expansions for w in Eqs. (6) and (8) satisfy the periodicity conditions (21) exactly for $0 \leqslant x \leqslant 2L$, as well as the essential boundary conditions (5a) or (5b).

The velocity potential can be assumed to be of the form

$$\Phi(x, r, \theta, t) = \eta(r)\xi(x)g(\theta)\zeta(t). \tag{25}$$

Substituting in Eq. (17) and using the method of separation of variables, one eventually finds

$$\eta(r) = A_m \mathrm{I}_n(k_m r) + B_m \mathrm{K}_n(k_m r), \tag{26}$$

$$\xi(x) = C_m \sin(k_m x) + D_m \cos(k_m x), \tag{27}$$

$$g(\theta) = J \cos(n\theta) + H \sin(n\theta), \tag{28}$$

where A_m, B_m, D_m, E_m, J and H are constants, and $I_n(\ )$ and $K_n(\ )$ are the modified Bessel functions of the first and second kind and order n. The constants A_m and B_m are found by using Eq. (23) or Eq. (24) for internal or

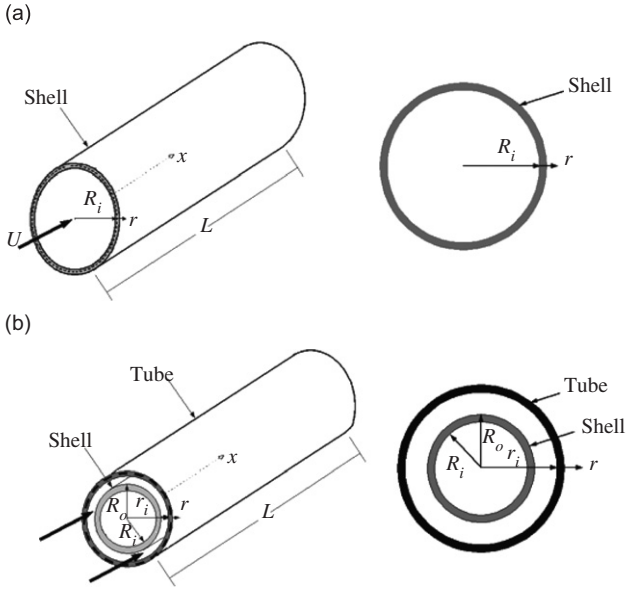

Fig. 3. Shell configuration for the radial boundary conditions: (a) internal flow and (b) annular flow.

annular flow, respectively. In the CC model the determination of constants C_m and D_m in Eq. (27) is rather complicated since the radial boundary conditions for internal or annular flow require that the x-dependent function in w, given in Eq. (6), have the same argument (wavelength) as the x-dependent solution of the velocity potential in Eq. (27). This is impossible to establish directly since the beam eigenfunctions for clamped–clamped boundary conditions are utilized, which contain hyperbolic functions with "wavenumber" λ_m (see Eq. (7)), while equation (27) is a linear combination of sine and cosine functions of wavenumber k_m. To circumvent this problem, the radial deformation for the flow boundary (i.e., the shell interface) is expanded as a Fourier sine series, transforming the beam functions of Eq. (7) into a sine series of exactly the same wavenumber, k_m. Therefore, the general form of the solution for w is given by

$$\begin{aligned} w(x,\theta,t) &= \sum_{m=1}^{M}\sum_{n=0}^{N} w_{m,n}(x,\theta,t) \\ &= \sum_{m=1}^{M}\sum_{n=0}^{N}\sum_{j=1}^{KK} b_{m,j}\sin(j\pi x/L)[A_{m,n}(t)\cos(n\theta)+B_{m,n}(t)\sin(n\theta)], \end{aligned} \tag{29}$$

where M, N *and* KK are integers, $\theta = y/R$ and

$$b_{m,j} = \frac{2}{L}\sum_{j=1}^{KK}\int_0^L \varphi_m(x)\sin(j\pi x/L)\mathrm{d}x, \tag{30}$$

in which $\varphi_m(x)$ are the beam eigenfunctions given in Eq. (7).

The mode expansion in Eq. (29) involves the m and n indices that are explicitly used on the right-hand side of Eqs. (6) and (12). The reason for this is that in Eq. (30) the transformation of the radial deformation w must be done for each term of the solution expansion separately. That is, each of the asymmetric modes (driven and companion) and axisymmetric modes involved in the mode expansion (12) must be transformed to the new solution expansion given in Eq. (29) individually. The unknown wavenumber k_m is then calculated by using the radial boundary condition for either internal or annular flow. Since there is a finite summation of terms in Eq. (29), there will be a relative error associated with the number of terms retained in Eq. (29), which should be minimized. For the seven dof model, 60 terms is found to be adequate.

In the case of the SS (simply supported shell) model, the determination of the constants C_m and D_m in Eq. (27) is simple, since the solution expansion for simply supported shells given in Eq. (8) involves the same argument (wavelength) as the x-dependent solution of the velocity potential in Eq. (27).

The solution of the velocity potential and perturbation pressure is found both for internal and for annular flow in the following two subsections.

2.4. Perturbation pressure for internal flow

Fig. 3(a) shows the cylindrical shell system subjected to internal flow. Using the first of the two radial boundary conditions in Eq. (23), one concludes that B_m must vanish. Therefore, the solution for $\eta(r)$ becomes

$$\eta_{m,n}(r) = A_m \mathrm{I}_n(k_m r). \tag{31}$$

In the CC model, k_m is evaluated by using the second radial boundary condition in Eq. (23). Substituting Eqs. (25) and (31) into (23) and rearranging the expression, one obtains the following relationship between the $\xi_m(x)$ and $w(x,\theta,t)$:

$$\sum_m \sum_n \xi_m(x) g_n(\theta) \zeta_{m,n}(t) [\mathrm{d}\eta_{m,n}(r)/\mathrm{d}r]_{r=R_i} = -[\partial w(x,\theta,t)/\partial t + U \partial w(x,\theta,t)\partial x]. \tag{32}$$

It is important to note that Eq. (32) holds true only if there is an one-to-one correspondence between each x-dependent term of the series taken from the left-hand side of the equation, i.e., the $\xi_m(x)$ term, to its corresponding x-dependent term on the right-hand side of the series expansion because of the orthogonality property of the $\xi_m(x)$. In addition, the wavenumbers related to the solution in the x-direction, that is $\xi_m(x)$ and $w(x,\theta,t)$, must be exactly the same for physical and mathematical justification of Eq. (31). Therefore, for internal flow, the value of k_m is given by

$$k_m = \frac{m\pi}{L}, \quad m = 1, 2, 3, \ldots \tag{33}$$

Using Eqs. (25), (29), (30) and (32), the velocity potential is given by

$$\begin{aligned} \Phi = & -\sum_{m=1}^{M} \sum_{n=0}^{N} \sum_{j=1}^{KK} \frac{\mathrm{I}_n(k_m r)}{k_m \mathrm{I}'_n(k_m r)\big|_{r=R}} [\cos(n\theta) + \sin(n\theta)] \\ & \times [b_{m,j} \sin(m\pi x/L) \dot{\zeta}_{m,n}(t) + U b_{m,j} (m\pi/L) \cos(m\pi x/L) \zeta_{m,n}(t)], \end{aligned} \tag{34}$$

where I'_n is the derivative of I_n with respect to its argument and the overdot denotes differentiation with respect to t; moreover, $\zeta_{m,n}(t)$ is replaced by $A_{m,n}(t)$ when multiplied by $\cos(n\theta)$ and by $B_{m,n}(t)$ when multiplied by $\sin(n\theta)$.

The final general expression for the perturbation pressure at the shell surface is given by substituting Eq. (34) into Eq. (20) to obtain

$$\begin{aligned} p = & \rho_F \sum_{m=1}^{M} \sum_{n=0}^{N} \sum_{j=1}^{KK} \frac{\mathrm{I}_n(k_m R_i)}{k_m \mathrm{I}'_n(k_m r)\big|_{r=R_i}} [\cos(n\theta) + \sin(n\theta)] \\ & \times \Big[b_{m,j} \sin(m\pi x/L) \ddot{\zeta}_{m,n}(t) + 2U b_{m,j} (m\pi/L) \cos(m\pi x/L) \dot{\zeta}_{m,n}(t) \\ & - U^2 (m\pi/L)^2 b_{m,j} \sin(m\pi x/L) \zeta_{m,n}(t) \Big] \\ = & \rho_F \sum_{m=1}^{M} \sum_{n=0}^{N} \frac{\mathrm{I}_n(k_m R_i)}{k_m \mathrm{I}'_n(k_m r)\big|_{r=R_i}} \left(\frac{\partial}{\partial t} + U \frac{\partial}{\partial x} \right)^2 w_{m,n}. \end{aligned} \tag{35}$$

In the case of the simply supported shell, the expansion in Eq. (8) along with the second radial boundary condition (23) and Eq. (25) are used to obtain the general solution of the velocity potential:

$$\Phi = -\sum_{m=1}^{M} \sum_{n=0}^{N} \frac{L}{m\pi} \frac{\mathrm{I}_n(m\pi r/l)}{\mathrm{I}'_n(m\pi R_i/L)} \left(\frac{\partial w_{m,n}}{\partial t} + U \frac{\partial w_{m,n}}{\partial x} \right), \tag{36}$$

where $w \equiv w_{m,n}$ is given in Eq. (8). In the SS model, the final expression for the internal perturbation pressure at the shell surface is found by substituting Eq. (36) into Eq. (20) to obtain

$$p = \rho_F \sum_{m=1}^{M} \sum_{n=0}^{N} \frac{L}{m\pi} \frac{\mathrm{I}_n(m\pi r/L)}{\mathrm{I}'_n(m\pi R_i/L)} \left(\frac{\partial}{\partial t} + U \frac{\partial}{\partial x} \right)^2 w_{m,n}. \tag{37}$$

2.5. Perturbation pressure for annular flow

Applying the first radial boundary condition (24a), the solution of Eq. (26) becomes

$$\eta_{m,n}(r) = B_m \left[\frac{\mathrm{K}_{n-1}(k_m r_i) + \mathrm{K}_{n+1}(k_m r_i)}{\mathrm{I}_{n-1}(k_m r_i) + \mathrm{I}_{n+1}(k_m r_i)} \right] \mathrm{I}_n(k_m r) + B_m \mathrm{K}_n(k_m r). \tag{38}$$

Then, proceeding in a completely analogous manner as in Section 2.4, one obtains

$$\begin{aligned} \Phi = & -\sum_{m=1}^{M} \sum_{n=0}^{N} \sum_{j=1}^{KK} \frac{\left\{ \left[\frac{\mathrm{K}_{n-1}(k_m r_i) + \mathrm{K}_{n+1}(k_m r_i)}{\mathrm{I}_{n-1}(k_m r_i) + \mathrm{I}_{n+1}(k_m r_i)} \right] \mathrm{I}_n(k_m r)\big|_{r=R_o} + \mathrm{K}_n(k_m r)\big|_{r=R_o} \right\} [\cos(n\theta) + \sin(n\theta)]}{k_m \left[\frac{\mathrm{K}_{n-1}(k_m r_i) + \mathrm{K}_{n+1}(k_m r_i)}{\mathrm{I}_{n-1}(k_m r_i) + \mathrm{I}_{n+1}(k_m r_i)} \right] \mathrm{I}'_n(k_m r)\big|_{r=R_o} + k_m \mathrm{K}'_n(k_m r)\big|_{r=R_o}} \\ & \times [b_{m,j} \sin(m\pi x/L) \dot{\zeta}_{m,n}(t) + U b_{m,j} (m\pi/L) \cos(m\pi x/L) \zeta_{m,n}(t)], \end{aligned} \tag{39}$$

where the prime and overdot are as in Eq. (34).

The final expression for the perturbation pressure in annular flow at the surface of the shell is obtained by substituting Eq. (39) into Eq. (20) and is given by

$$\begin{aligned} p = & \rho_F \sum_{m=1}^{M} \sum_{n=0}^{N} \sum_{j=1}^{KK} \frac{\left\{ \left[\frac{\mathrm{K}_{n-1}(k_m r_i) + \mathrm{K}_{n+1}(k_m r_i)}{\mathrm{I}_{n-1}(k_m r_i) + \mathrm{I}_{n+1}(k_m r_i)} \right] \mathrm{I}_n(k_m r)\big|_{r=R_o} + \mathrm{K}_n(k_m r)\big|_{r=R_o} \right\} [\cos(n\theta) + \sin(n\theta)]}{k_m \left[\frac{\mathrm{K}_{n-1}(k_m r_i) + \mathrm{K}_{n+1}(k_m r_i)}{\mathrm{I}_{n-1}(k_m r_i) + \mathrm{I}_{n+1}(k_m r_i)} \right] \mathrm{I}'_n(k_m r)\big|_{r=R_o} + k_m \mathrm{K}'_n(k_m r)\big|_{r=R_o}} \\ & \times \Big[b_{m,j} \sin(m\pi x/L) \ddot{\zeta}_{m,n}(t) + U b_{m,j} (m\pi/L) \cos(m\pi x/L) \dot{\zeta}_{m,n}(t) \\ & + U (m\pi/L) b_{m,j} \cos(m\pi x/L) \dot{\zeta}_{m,n}(t) - U^2 (m\pi/L)^2 b_{m,j} \sin(m\pi x/L) \zeta_{m,n}(t) \Big], \end{aligned} \tag{40}$$

which could also be expressed as in the final line of Eq. (35). For a shell with simply supported ends in annular flow, a similar expression for the perturbation pressure may be obtained.

2.6. Method of solution

This section of the paper presents the solution techniques employed to solve for the generalized coordinates of the mode expansions. First, the solution of the structural part of the model given in Eqs. (1) and (2) is presented, followed in Section 2.6.2 by the solution method used for cases with fluid–structure interaction. In Sections 2.6.3, 2.7 and 2.8, the discretization of the partial differential equation of motion, incorporation of a possible transmural pressure acting on the shell, non-dimensionalization, and the numerical scheme used for time integration are presented for the CC and SS models.

2.6.1. Solution of the structural model

A numerical technique is used to discretize the equation and obtain a set of ordinary differential equations. Prior to this, the Airy stress function F must be defined using Eq. (2); it is then substituted into Eq. (1) to solve for the unknowns of the mode expansion for w.

The solution of F can be obtained from Eq. (2) using averaging methods or a closed form solution. In this work, F was calculated using an exact technique without any approximation. The solution of F is composed of a particular solution F_p and a homogeneous solution F_h,

$$F = F_h + F_p. \tag{41}$$

To find the particular solution, the mode expansion w is substituted into Eq. (2). In the seven dof CC model, this gives 280 terms in the particular solution, by ensuring the correspondence (one by one) between the right-hand side terms of Eq. (2) with appropriate solution terms on the left-hand side of the same expression. This is an arduous task, fraught with numerical difficulties, because of the hyperbolic functions involved in the modal expansion. The expression for F_p involves the beam eigenfunctions explicitly, as shown in the equation below:

$$\begin{aligned}\nabla^4 F_p = \frac{Eh}{R^2}\{&n^2\big[(B_{1,n}(t)\cos(ny/R) - A_{1,n}(t)\sin(ny/R))\phi_1'(x)\\&+(B_{2,n}(t)\cos(ny/R) - A_{2,n}(t)\sin(ny/R))\phi_2'(x)\big]^2\\&- R\big[(A_{1,0}(t) + A_{1,n}(t)\cos(ny/R) + B_{1,n}(t)\sin(ny/R))\phi_1''(x)\\&+(A_{2,n}(t)\cos(/R) + B_{2,n}(t)\sin(ny/R))\phi_2''(x) + A_{3,0}(t)\phi_3''(x) + A_{5,0}(t)\phi_5''(x)\big]\\&+ n^2\big[(A_{1,n}(t)\cos(ny/R) + B_{1,n}(t)\sin(ny/R))\phi_1(x)\\&+(A_{2,n}(t)\cos(ny/R) + B_{2,n}(t)\sin(ny/R))\phi_2(x)\big]^2\\&\times\big[(A_{1,0}(t) + A_{1,n}(t)\cos(ny/R) + B_{1,n}(t)\sin(ny/R))\phi_1''(x)\\&+(A_{2,n}(t)\cos(ny/R) + B_{2,n}(t)\sin(ny/R))\phi_2''(x)+A_{3,0}(t)\phi_3''(x) + A_{5,0}(t)\phi_5''(x)\big]\},\end{aligned} \tag{42}$$

where the prime denotes differentiation with respect to x. Eq. (42) is further expanded using trigonometric relations, after substituting in it the expressions for the eigenfunctions given in Eq. (7). The final form of F_p for clamped–clamped shells is given in Ref. [37].

In the seven dof SS model, the simpler expansion given in Eq. (8) is used along with Eq. (2) to calculate F_p, which is found to be [34]

$$\begin{aligned}F_p = \sum_{m=0}^{M}\sum_{n=0}^{N}\{&[F_{1mn}\cos(ny/R) + F_{2mn}\sin(ny/R)]\sin(m\pi x/L)\\&+[F_{3mn}\cos(ny/R) + F_{4mn}\sin(ny/R)]\cos(m\pi x/L)\},\end{aligned} \tag{43}$$

where the functions of time F_{jmn}, $j = 1,\ldots,4$, are given in Ref. [29].

Once the particular solution F_p is found for both CC and SS models, the homogeneous solution of F is calculated using the following assumed form:

$$\begin{aligned}F_h = &\left\{\frac{1}{2}\left(\bar{N}_x - \frac{1}{2\pi RL}\int_0^{2\pi R}\int_0^{L}\left[\frac{\partial^2 F_p}{\partial y^2}\right]\mathrm{d}y\,\mathrm{d}x\right)y^2\right\} + \left\{\frac{1}{2}\left(\bar{N}_y - \frac{1}{2\pi RL}\int_0^{2\pi R}\int_0^{L}\left[\frac{\partial^2 F_p}{\partial x^2}\right]\mathrm{d}y\,\mathrm{d}x\right)x^2\right\}\\&-\left\{\left(\bar{N}_{xy} - \frac{1}{2\pi RL}\int_0^{2\pi R}\int_0^{L}\left[\frac{\partial^2 F_p}{\partial x\partial y}\right]\mathrm{d}y\,\mathrm{d}x\right)xy\right\},\end{aligned} \tag{44}$$

where $\bar{N}_x$, $\bar{N}_y$ and $\bar{N}_{xy}$ are the averaged in-plane restraint stresses. The homogeneous solution of F given in Eq. (44) is not the most general expression possible, but it is sufficient to satisfy boundary conditions (3) on average. This is true since the contribution of F_p to the F_h expression for all the in-plane stresses is averaged over the length and circumference of the shell as in Eq. (44). For the CC model, utilizing Eqs. (9)–(11) along with (4), the averaged in-plane stresses are given by the following expressions:

$$\bar{N}_x = \frac{Eh}{(1-\nu^2)}\frac{1}{2\pi RL}\int_0^{L}\int_0^{2\pi R}\left(-\frac{\nu w}{R} + \frac{1}{2}\left(\frac{\partial w}{\partial x}\right)^2 + \frac{\nu}{2}\left(\frac{\partial w}{\partial y}\right)^2\right)\mathrm{d}y\,\mathrm{d}x, \tag{45a}$$

$$\bar{N}_y = \frac{Eh}{(1-\nu^2)}\frac{1}{2\pi RL}\int_0^{L}\int_0^{2\pi R}\left(-\frac{w}{R} + \frac{\nu}{2}\left(\frac{\partial w}{\partial x}\right)^2 + \frac{1}{2}\left(\frac{\partial w}{\partial y}\right)^2\right)\mathrm{d}y\mathrm{d}x, \tag{45b}$$

$$\bar{N}_{xy} = \frac{Eh}{(1+\nu)}\frac{1}{\pi RL}\int_0^{L}\int_0^{2\pi R}\left(\frac{\partial w}{\partial x}\frac{\partial w}{\partial y}\right)\mathrm{d}y\mathrm{d}x. \tag{45c}$$

The contribution of F_p to $\bar{N}_x$ and $\bar{N}_{xy}$ is zero. The corresponding expressions for the SS model are given in Amabili et al. [29]. Once Eq. (44) is expanded, F_h is added to F_p for the total expression of the Airy stress function, as in Eq. (41). In the seven dof CC model the total solution of F is composed of 310 terms, involving complicated trigonometric functions.

Once the solution for F has been obtained for each model, Eq. (41) is substituted into Eq. (1) along with the corresponding expression for w given in Eqs. (6) and (8). Eq. (1) now contains only the structural part of the original equation of motion (p is added to the equation of motion separately later) and is discretized to seven ordinary differential equations using the Galerkin technique with comparison functions $\phi_i(x, y)$. In the CC model, the comparison functions chosen are the eigenfunctions for a clamped–clamped beam, while in the SS model they are the corresponding ones for a simply supported beam. The general form of the comparison functions is

$$\phi_i(x,y) = \left\{ \begin{array}{c} \phi_1 = \varphi_1 \cos(ny/R) \\ \phi_2 = \varphi_1 \sin(ny/R) \\ \phi_3 = \varphi_2 \cos(ny/R) \\ \phi_4 = \varphi_2 \sin(ny/R) \\ \phi_5 = \varphi_1 \\ \phi_6 = \varphi_3 \\ \phi_7 = \varphi_5 \end{array} \right\}, \tag{46}$$

where in the CC model φ_i are defined in Eq. (7), and in the SS model they are $\sin(i\pi x/L)$, $i = 1, 2, 3, 5$.

Therefore, the seven ordinary differential equations, for the CC and the SS models, are obtained by using Eqs. (1) and (46) into a Galerkin scheme of the form

$$\mathrm{ODE}(i) = \int_0^L \int_0^{2\pi R} [\text{Eq. (50)}]\phi_i(x,y)\,\mathrm{d}y\,\mathrm{d}x \quad \text{for} \quad i = 1 \ldots 7. \tag{47}$$

In the case of the CC model, the final form for the seven ordinary differential equations is given as follows. The first equation for $\phi_1(x, y)$ projection is

$$\begin{aligned} & m_{1,n}\ddot{A}_{1,n}(t) + c_{1,n}\dot{A}_{1,n}(t) + k_{1,n}A_{1,n}(t) + \alpha_1 A_{1,n}(t)A_{1,0}(t) + \alpha_2 A_{1,n}(t)A_{1,0}^2(t) + \alpha_3 A_{1,n}^3(t) \\ & \quad + \alpha_4 A_{1,n}^2(t)A_{2,n}(t) + \alpha_5 A_{1,n}(t)A_{2,n}^2(t) + \alpha_6 A_{2,n}^3(t) + \alpha_7 A_{1,n}(t)A_{3,0}(t) \\ & \quad + \alpha_8 A_{1,n}(t)A_{1,0}(t)A_{3,0}(t) + \alpha_9 A_{2,n}(t)A_{3,0}(t) + \alpha_{10} A_{2,n}(t)A_{1,0}(t)A_{3,0}(t) \\ & \quad + \alpha_{11} A_{1,n}(t)A_{3,0}^2(t) + \alpha_{12} A_{2,n}(t)A_{3,0}^2(t) + \alpha_{13} A_{1,n}(t)A_{5,0}(t) + \alpha_{14} A_{1,0}(t)A_{1,n}(t)A_{5,0}(t) \\ & \quad + \alpha_{15} A_{2,n}(t)A_{5,0}(t) + \alpha_{16} A_{2,n}(t)A_{1,0}(t)A_{5,0}(t) + \alpha_{17} A_{1,n}(t)A_{3,0}(t)A_{5,0}(t) \\ & \quad + \alpha_{18} A_{2,n}(t)A_{3,0}(t)A_{5,0}(t) + \alpha_{19} A_{1,n}(t)A_{5,0}^2(t) + \alpha_{20} A_{2,n}(t)A_{5,0}^2(t) + \alpha_{21} A_{1,n}(t)B_{1,n}^2(t) \\ & \quad + \alpha_{22} A_{2,n}(t)B_{1,n}^2(t) + \alpha_{23} A_{1,n}(t)B_{1,n}(t)B_{2,n}(t) + \alpha_{24} A_{2,n}(t)B_{1,n}(t)B_{2,n}(t) \\ & \quad + \alpha_{25} A_{1,n}(t)B_{2,n}^2(t) + \alpha_{26} A_{2,n}(t)B_{2,n}^2(t) = 0, \end{aligned} \tag{48}$$

where $m_{1,n}$ is the modal mass coefficient after the Galerkin projection, $c_{1,n}$ the corresponding modal damping coefficient, $k_{1,n}$ the modal stiffness coefficient and $\alpha_i (i = 1 \ldots 26)$ are coefficients that depend on the projection of the radial deformation and Airy stress solution of Eq. (1) as a function of material properties, shell geometry and the value of the wavenumber n. The other six equations associated with the seven dof model are given in Appendix A.1. The final form of Eq. (48) can be integrated numerically in time to obtain the phase portrait of the amplitude functions over time.

In the SS model, the seven ordinary differential equations have been obtained in a similar fashion by Amabili et al. [29] and will not be reproduced in this paper.

2.6.2. Solution for the perturbation pressure for internal flow

The perturbation pressure of the internal flow is calculated using Eq. (35) for the CC model and Eq. (37) for the SS model, along with the corresponding comparison functions in Eq. (46). The resulting Galerkin expression is given by

$$p_i^{\text{internal}} = \int_0^L \int_0^{2\pi R} [p^{\text{internal}}]\phi_i(x,y)\,\mathrm{d}y\,\mathrm{d}x, \quad i = 1\ldots 7, \tag{49}$$

where p^{internal} is given in Eq. (35) for the CC model or Eq. (37) for the SS model. The perturbation pressure comprises two contributions:

$$p^{\text{internal}} = p^{\text{internal}}_{\text{asymmetric}} + p^{\text{internal}}_{\text{axisymmetric}}, \tag{50}$$

where in the CC model $p^{\text{internal}}_{\text{asymmetric}}$ and $p^{\text{internal}}_{\text{axisymmetric}}$ are given below:

$$\begin{aligned} p^{\text{internal}}_{\text{asymmetric}} = \sum_{m=1}^{MM} & \rho_F[2L\mathrm{I}_n(m\pi R/R)/(m\pi \mathrm{I}_{n-1}(m\pi R/L) + \mathrm{I}_{n+1}(m\pi R/L))] \\ & \times \big[(\ddot{A}_{1,n}(t)\cos(ny/R) + \ddot{B}_{1,n}(t)\sin(ny/R))\psi_1 \sin(m\pi x/L) \\ & + (\ddot{A}_{2,n}(t)\cos(ny/R) + \ddot{B}_{2,n}(t)\sin(ny/R))\psi_2 \sin(m\pi x/L) \\ & + (\dot{A}_{1,n}(t)\cos(ny/R) + \dot{B}_{1,n}(t)\sin(ny/R))\psi_1 (2Um\pi/L)\cos(m\pi x/L) \\ & + (\dot{A}_{2,n}(t)\cos(ny/R) + \dot{B}_{2,n}(t)\sin(ny/R))\psi_2 (2Um\pi/L)\cos(m\pi x/L) \\ & - (A_{1,n}(t)\cos(ny/R) + B_{1,n}(t)\sin(ny/R))\psi_1 (U^2m^2\pi^2/L^2)\sin(m\pi x/L) \\ & -(A_{2,n}(t)\cos(ny/R) + B_{2,n}(t)\sin(ny/R))\psi_2 (U^2m^2\pi^2/L^2)\sin(m\pi x/L)\big], \end{aligned} \tag{51}$$

where $\Psi_1 = \frac{2}{L}\int_0^L \varphi_1 \sin(m\pi x/L)\,\mathrm{d}x$, $\psi_2 = \frac{2}{L}\int_0^L \varphi_2 \sin(m\pi x/L)\mathrm{d}x$; and

$$\begin{aligned} p^{\text{internal}}_{\text{axisymmetric}} = \sum_{m=1}^{MM} & \rho_F(LI_0(m\pi R/L)/m\pi I_1(m\pi R/L)) \\ & \times \big[(\ddot{A}_{1,0}(t)\psi_1 + \ddot{A}_{3,0}(t)\psi_3 + \ddot{A}_{5,0}(t)\psi_5)\sin(m\pi x/L) \\ & + (\dot{A}_{1,0}(t)\psi_1 + \dot{A}_{3,0}(t)\psi_3 + \dot{A}_{5,0}(t)\psi_5)(2Um\pi/L)\cos(m\pi x/L) \\ & -(A_{1,0}(t)\psi_1 + A_{3,0}(t)\psi_3 + A_{5,0}(t)\psi_5)U^2(m\pi/L)^2\sin(m\pi x/L)\big], \end{aligned} \tag{52}$$

where

$$\psi_3 = \frac{2}{L}\int_0^L \varphi_3 \sin(m\pi x/L)\,\mathrm{d}x \quad \text{and} \quad \psi_5 = \frac{2}{L}\int_0^L \varphi_5 \sin(m\pi x/L)\,\mathrm{d}x.$$

For the SS model, $p^{\text{internal}}_{\text{asymmetric}}$ and $p^{\text{internal}}_{\text{axisymmetric}}$ are given in Appendix A.2.

2.6.3. Solution for the perturbation pressure for annular flow

The perturbation pressure for the annular flow consists of the contributions of the asymmetric and the axisymmetric modes involved in the solution of the velocity potential. Therefore, the total perturbation pressure for the CC model given in Eq. (40) can be expressed as

$$p^{\text{annular}} = p^{\text{annular}}_{\text{asymmetric}} + p^{\text{annular}}_{\text{axisymmetric}}. \tag{53}$$

The expressions for p^{annular} for the CC model are given in Appendix A.3. The expression for the perturbation pressure for a shell with simply supported ends subjected to annular flow is given in Amabili et al. [34].

2.7. Computation of the transmural pressure

In some of the experiments (Section 4), a mean inwards pressurization $\Delta P_{tm}(x)$ was applied at shell midlength. However, the theory developed thus far does not include transmural pressurization.

Hence, additional terms must be added to the equation of motion. For the seven dof model, after Galerkin projection, the following terms must be included, one to each of the seven ordinary differential equations (ODEs) of the discretized system:

$$\left\{\begin{array}{ll} \bar{p}_1 = \int_0^L \int_0^{2\pi R} (P_{\exp}\varphi_1 \cos(ny/R))\,\mathrm{d}y\,\mathrm{d}x = 0, & \bar{p}_2 = \int_0^L \int_0^{2\pi R} P_{\exp}\varphi_1 \sin(ny/R)\,\mathrm{d}y\,\mathrm{d}x = 0 \\ \bar{p}_3 = \int_0^L \int_0^{2\pi R} \left(P_{\exp}\varphi_2 \cos\left(ny/R\right)\right)\mathrm{d}y\,\mathrm{d}x = 0, & \bar{p}_4 = \int_0^L \int_0^{2\pi R} P_{\exp}\varphi_2 \sin(ny/R)\,\mathrm{d}y\,\mathrm{d}x = 0, \\ \bar{p}_5 = \int_0^L \int_0^{2\pi R} (P_{\exp}\varphi_1)\,\mathrm{d}y\,\mathrm{d}x, & \bar{p}_6 = \int_0^L \int_0^{2\pi R} (P_{\exp}\varphi_3)\,\mathrm{d}y\,\mathrm{d}x \\ \bar{p}_7 = \int_0^L \int_0^{2\pi R} (P_{\exp}\varphi_5)\,\mathrm{d}y\,\mathrm{d}x, & \end{array}\right\}, \tag{54}$$

where $P_{\exp}$ is the magnitude of the transmural pressure applicable in a given experiment.

2.8. Non-dimensionalization of the equation of motion

The form of the final equation of motion is obtained with the inclusion of p in Eq. (1). In this analysis f is set equal to zero. It is useful to rewrite the final equations of motion in non-dimensional form. The following scheme is adopted:

$$\tau = \omega_{1,n} t, \quad \tilde{A}_{m,n}(\tau) = A_{m,n}(t)/h, \quad \tilde{B}_{m,n}(\tau) = B_{m,n}(t)/h, \tag{55}$$

where $\omega_{1,n}$ is the fundamental frequency of the linear equations of motion for the first radial mode, and h is the shell thickness. The final equations of motion (including the perturbation pressure) were non-dimensionalized by dividing them by $\omega_{1,n}^2 h$. In particular, the structural damping term is non-dimensionalized as follows:

$$\zeta_{m,n} = c_{m,n} h(\pi RL/2)/(2\omega_{1,n} m_{m,n}), \tag{56}$$

where in the CC model $c_{m,n}$ and $m_{m,n}$ are taken from Eq. (48), and in the SS model these coefficients are given in Amabili et al. [29]. Also, the flow velocity is non-dimensionalized using the definition of Weaver and Unny [9] via the following expression:

$$V = U/[\pi^2 \sqrt{D/\rho h}/L], \tag{57}$$

where U is the mean dimensional flow velocity and D is the flexural rigidity of the shell defined in the equation of motion (1).

2.9. Numerical integration of the equations of motion

The partial differential equations of motion were discretized to the seven second-order ordinary differential equations of motion, Eqs. (48), (50) and (53) via a Galerkin technique, using the Mathematica Version 4 computer software [47], by performing analytical surface integrals of trigonometric functions.

The discretized equations were then transformed into two first-order equations and transferred to a Fortran file. The resulting first-order ordinary differential equations are studied by using the AUTO 97 [48] software for continuation and bifurcation analysis of nonlinear ordinary differential equations via pseudo-arclength continuation and collocation methods.

In the case of fluid–structure interaction, i.e., in the presence of internal or annular flow, the dimensionless flow velocity V is used as the bifurcation parameter. The solution followed all stability branches to obtain the final bifurcation diagrams of shell amplitude versus V, with indications on critical flow velocities and qualitative changes in the nonlinear shell behaviour.

Additional theoretical results, included in Section 3, were obtained using Gear's backward differentiation formula, verifying the results obtained with AUTO 97.

3. Nonlinear theoretical results for clamped shells

The seven dof CC model was used to investigate the nonlinear response of a clamped–clamped shell with internal fluid flow, and to study the stability of the shell. The shell used in the theoretical calculations

Table 1
Material properties for the shells used in the internal or annular air-flow experiments and internal water-flow experiments

Shell	E (N/m^2)	ρ_s (kg/m^3)	v
Elastomer	2.82×10^5	1.16×10^3	0.47
Aluminium	70×10^9	2.72×10^3	0.38
Plastic (PET)	2.3×10^9	0.8×10^3	0.4

E is Young's modulus, ρ_s the density of the material, and v the Poisson ratio.

Table 2
Shell dimensions for the elastomer shells with internal or annular air-flow and the aluminium and PET shells with internal water-flow tests

Shell system	Length (mm)	External diameter (mm)	Thickness (mm)	L/R
Internal air-flow	40	51.20	1.5	1.7
Annular air-flow	104.3	50.09	1.5	2.0
Aluminium water flow	122.5	82.25	0.137	2.98
PET water flow	100.1	83.6	0.300	2.41

(corresponding to one used in the experiments) is made of Polyethylene-Terephthalate (PET) with material properties and dimensions listed in Tables 1 and 2, respectively. The fluid is water with a density of $\rho_F = 1000\,\text{kg/m}^3$. The clamped PET shell is positioned within a concentric tube that provides an annular space with internal diameter of 203 mm, filled with quiescent water. The transmural pressure between the internal and annular space was set equal to zero for this numerical investigation.

Because of AUTO software limitations (to be discussed later) the companion modes were eliminated in these calculations from the mode expansion, leaving only the two driven asymmetric modes and three longitudinal axisymmetric ones. Therefore, the seven dof model is reduced to a five dof model. All theoretical results in this section have been computed for $n = 6$ (corresponding to the experimental results in Ref. [40]).

The results for all the modal amplitudes versus the non-dimensional internal flow velocity, are shown in Fig. 4. It is seen in Fig. 4 that the shell loses stability by divergence at a critical flow velocity of $V_c = 1.89$. At this flow velocity, according to the results for the first asymmetric mode $A_{1,6}(t)$ shown in Fig. 4(a), after losing stability the system follows the unstable part of Branch 2. At $V = 1.2$ the solution reaches the limit point at which it folds and changes to a stable Branch 2 solution, the amplitude of which increases with increasing flow velocity. The second asymmetric mode $A_{2,6}(t)$ indicates that, beyond the first bifurcation point (beyond V_c) there is a second bifurcation, at $V = 2.09$ (Fig. 4(b)). The system then follows the unstable Branch 3 until it folds at $V = 1.13$ and becomes stable. It is interesting to note that the folding of Branch 3 occurs at a smaller flow velocity than the folding of Branch 2 for $A_{1,6}(t)$. The response curves of both driven asymmetric modes are symmetrical *vis-à-vis* the zero amplitude axis, as shown in Fig. 4(a,b).

The response component associated with the first axisymmetric mode $A_{1,0}(t)$, shown in Fig. 4(c), indicates that this mode contributes only to radial contraction of the shell: both bifurcation points at $V = 1.89$ (Branch 2) and $V = 2.09$ (Branch 3) generate subcritical response curves with positive values. In this case the response of Branch 3 is more subcritical but with smaller amplitude values. In the case of the third axisymmetric mode (Fig. 4(d)), $A_{3,0}(t)$, the solutions generated by the two aforementioned bifurcation points have opposite signs. The first bifurcation point gives a negative solution Branch 2, with amplitude values smaller than the positive solution of Branch 3. The fifth longitudinal axisymmetric mode, $A_{5,0}(t)$, provides two solution branches that have negative values (Fig. 4(e)), associated with small expansion of the shell wall outwards. Using the results of Fig. 4, the overall response of the PET shell subjected to water flow can be obtained. Fig. 5 shows the response amplitude at $x = L/3$ and $y = 0$ as a function of V. It is seen that the shell loses stability by divergence, and only static (non-oscillatory) solutions are present for the velocity range used in the theoretical calculations. The behaviour of the shell is strongly subcritical with a large hysteresis between the onset and folding points (compare the buckling velocity of 1.89 of Branch 2 to the folding point velocity 1.2 of the same solution branch).

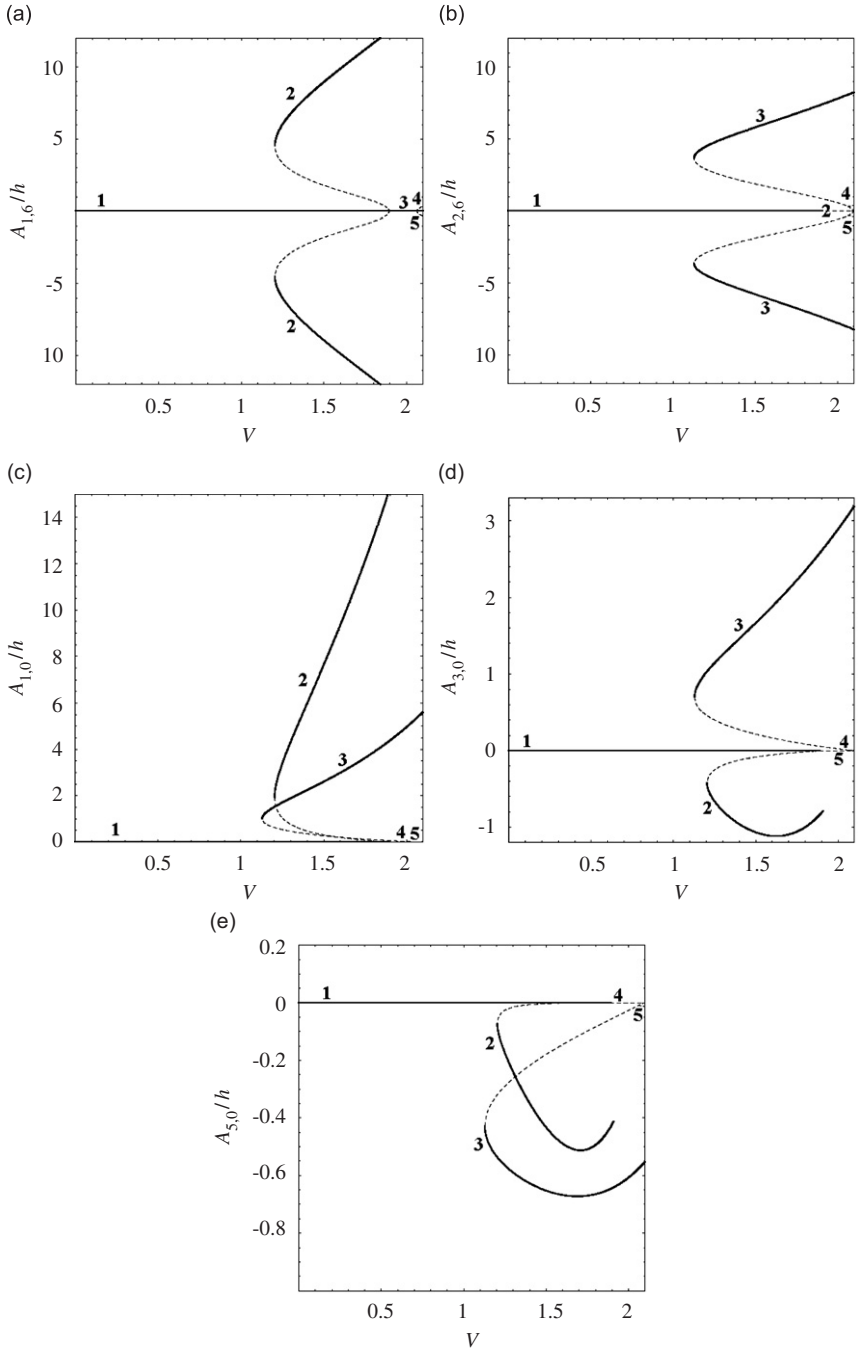

Fig. 4. Bifurcation diagram of the driven modes of the non-dimensional mode amplitude versus the non-dimensional flow velocity V of a clamped PET shell with internal water flow for $\Delta P_{tm} = 0$; ——, stable solution branches; – – – – –, unstable solution branches. Response of the amplitudes of (a) the first longitudinal asymmetric mode, $A_{1,6}/h$; (b) the second longitudinal asymmetric mode, $A_{2,6}/h$; (c) the first longitudinal axisymmetric mode, $A_{1,0}/h$; (d) the third longitudinal axisymmetric mode, $A_{3,0}/h$; (e) the fifth longitudinal axisymmetric mode, $A_{5,0}/h$.

Solution Branch 3 indicates a larger subcritical behaviour than Branch 2. This is an interesting phenomenon since it implies that, if the flow velocity is in the range of $1.13 < V < 2.09$, a small perturbation to the shell (for example, generated by a small flow perturbation) may force the system to jump from one stable solution

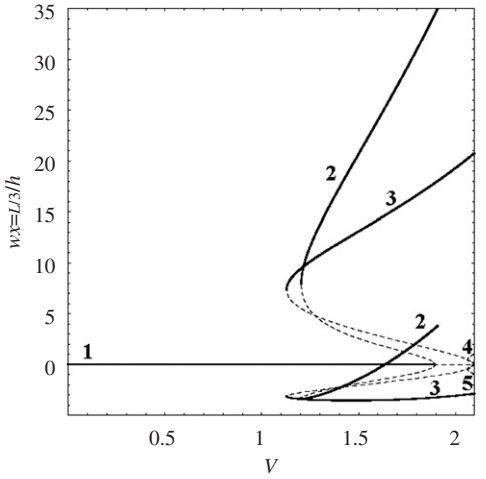

Fig. 5. Shell amplitude at $x = L/3$ and $y = 0$ versus the non-dimensional flow velocity V of the clamped PET shell of Fig. 4 with internal water flow, ————, Stable solution branches; - - - - - -, unstable solution branches; 1–5 indicate solution Branches 1–5.

to another (and back again). Moreover, if the solution lies on Branch 2 and the flow velocity is slowly decreased, there is a possibility of the system jumping to Branch 3, then folding at a smaller flow velocity than if the system had followed Branch 2. There is also a possibility that in this velocity range the shell solution could jump from the positive axis solutions of Branches 2 and 3 to the negative stable solutions of Branches 2 and 3; this would indicate a change from contraction to expansion of the shell wall.

It is noted that symmetry along the zero-amplitude axis observed in the amplitude solutions of the first two asymmetric modes, Fig. 4(a) and (b), does not appear in the overall shell response of Fig. 5 because of the asymmetrical contributions of the longitudinal axisymmetric modes. The amplitudes of solution Branch 2 keeps increasing with increasing flow velocity, diminishing the flow area inside the shell. The repercussions of such large shell deformations on the fluid flow within the shell should be recalled here [37,38,40]; moreover, it is not certain that the simple shell theory used is valid for such large deformations ($w/h \simeq 35$).

The response of the shell when the driven modes are replaced by the companion modes is exactly the same as in Fig. 4. The symmetry of the first two longitudinal asymmetric companion modes is retained and the final shell response corresponds to Fig. 5.

In the case of interaction between the orthogonal modes, modes rotated by $\pi/2n$, the results are shown in Fig. 6. In this case, modes $B_{1,6}(t)$ and $A_{2,6}(t)$ were set equal to zero throughout the time integration process in AUTO. The interaction between the orthogonal modes generated results that differ from those of Fig. 4. In this case, the first asymmetric driven mode $A_{1,6}(t)$ loses stability at $V = 1.89$ following the unstable solution Branch 2. At a flow velocity of 1.2, Branch 2 folds, but it remains unstable. Then there is another bifurcation point of Branch 2, and Branch 4 is generated. This new solution is unstable at first, until the flow velocity has reached the limit point at $V = 0.67$. After this, solution Branch 4 becomes stable and it increases with increasing flow velocity. Branch 5 is generated on the negative side of the amplitude axis from the negative symmetrical solution of Branch 2. Branch 3 is generated at the same bifurcation point that generated the unstable Branch 2. This is a much more complicated solution pattern than in Fig. 4. The complex behaviour produced from the interaction of the so-called orthogonal modes is also seen in the curve for the second companion asymmetric mode $B_{2,6}(t)$ in Fig. 6(b). The solution for this mode indicates that stable Branch 1 of the system bifurcates at two points: when $V = 1.89$ and 2.04. From the second bifurcation point, two unstable branches arise and, in contrast to the case of $A_{1,6}(t)$, Branch 2 now remains on the zero-amplitude axis and Branch 3 grows symmetrically relative to the V-axis. Nevertheless, even after reaching the limit point, Branch 3 remains unstable. Branches 4 and 5 that were generated from the earlier bifurcation point start as unstable solutions that fold at $V = 0.67$ and become stable thereafter. The amplitudes of the stable solutions of $B_{2,6}(t)$ are smaller than those for $A_{1,6}(t)$. In both cases the solutions are symmetrical about the zero-amplitude axis

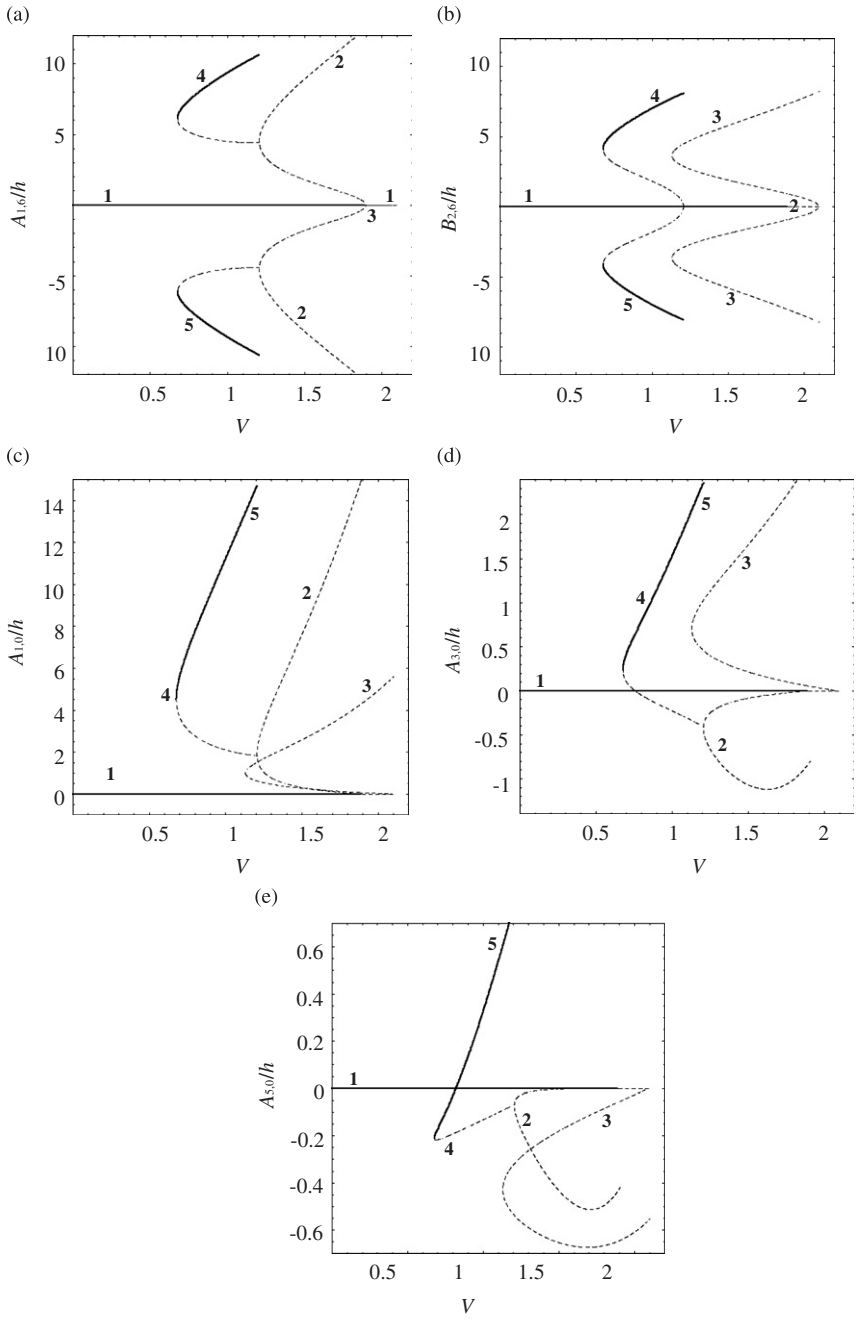

Fig. 6. Bifurcation diagram for a clamped PET shell with internal water flow, with $\Delta P_{tm} = 0$, of the non-dimensional mode amplitude versus the non-dimensional flow velocity V with interaction of the modes with $\pi/2n$ rotation. ————, Stable solution branches. – – – – –·, unstable solution branches Response of the amplitude of (a) the first longitudinal asymmetric mode, $A_{1,6}/h$; (b) the second companion longitudinal asymmetric mode, $B_{2,6}/h$; (c) the first longitudinal axisymmetric mode, $A_{1,0}/h$; (d) the third longitudinal axisymmetric mode, $A_{3,0}/h$; (e) the fifth longitudinal axisymmetric mode, $A_{5,0}/h$.

(V-axis). The response of the longitudinal axisymmetric modes $A_{1,0}(t)$, $A_{3,0}(t)$ and $A_{5,0}(t)$ are similarly complicated (Fig. 6(c)–(e)).

The total response of the mode expansion for this case at $x = L/3$ and $y = 0$ is shown in Fig. 7. These results show a very complex behaviour: for a wide range of flow velocities there are more than one stable solutions

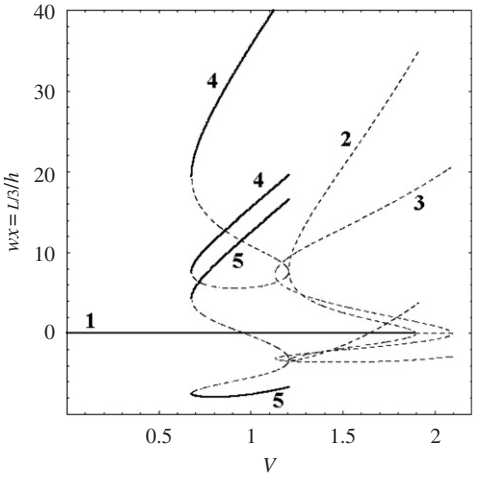

Fig. 7. Shell amplitude at $x = L/3$ and $y = 0$ versus the non-dimensional flow velocity V of the clamped PET shell of Fig. 6 in internal water flow with participation of companion modes. ————, Stable solution branches; – – – – –, unstable solution branches; 1–5 indicate solution Branches 1–5.

present, indicating possible jumps from one stable solution to another, assuming that enough perturbation is given to the system.

The AUTO software cannot follow the solution of the theoretical model when all the generalized coordinates (for both driven and companion modes) are present, since the solution evolves *on a surface* rather than in a plane. Therefore, a new computer code was written to (i) do such calculations and (ii) also confirm the results obtained by AUTO in the absence of the companion mode. The DIVPAG IMSL Fortran routine was utilized in a new computer code to perform the time integration for the unknown time functions. Fig. 8(a) shows the steady-state system response for the first asymmetric mode for various non-dimensional values of the flow velocity V. For values of V greater than 1.89 the solution of the first asymmetric mode follows a helicoidal motion revolving around the velocity axis. The subcritical response obtained by AUTO was also observed with the DIVPAG numerical package. In Fig. 8(b) the spiral-type solution of the first asymmetric mode is shown in a two-dimensional plot of $B_{1,6}(t)$ versus $A_{1,6}(t)$. The time history of the driven and companion modes of the first asymmetric mode for $V = 4.1$ is shown in Fig. 8(c). The time histories of all axisymmetric modes are shown in Fig. 8(d). Similar plots for the other shell cases (internal or annular fluid flow) have been obtained, and they agree with the results obtained by AUTO.

4. Experiments of clamped shells in axial fluid flow

Experiments were conducted in three different experimental set-ups, with shells of different materials, and with different flow configurations. Since some earlier but similar experiments are discussed in detail in Karagiozis et al. [40], the apparatus, and measuring techniques will be presented here in abbreviated form. Nevertheless, it should be made clear that the experimental results presented here are not those in the aforementioned reference; they correspond to another set of experiments, thus adding to the total experimental information in the literature.

The first set of experiments was conducted with elastomer shells in annular air-flow. The second was with elastomer shells with internal air-flow. The third and fourth sets were, respectively, with aluminium and plastic polyethylene terephthalate (PET) shells and internal water flow. The material properties and shell dimensions used in the experiments are listed in Tables 1 and 2, respectively.

In all experiments, instability in the form of divergence (buckling) developed abruptly, and hence it was necessary to capture its development carefully. For this, two different analogue non-contacting laser sensors along with a digital indicator controller and an analogue video camera were used. In the air-flow experiments, the MATSUSHITA ANR 1282 laser sensor with an output of 0–5 V and a resolution of 4/13/40 μm was used.

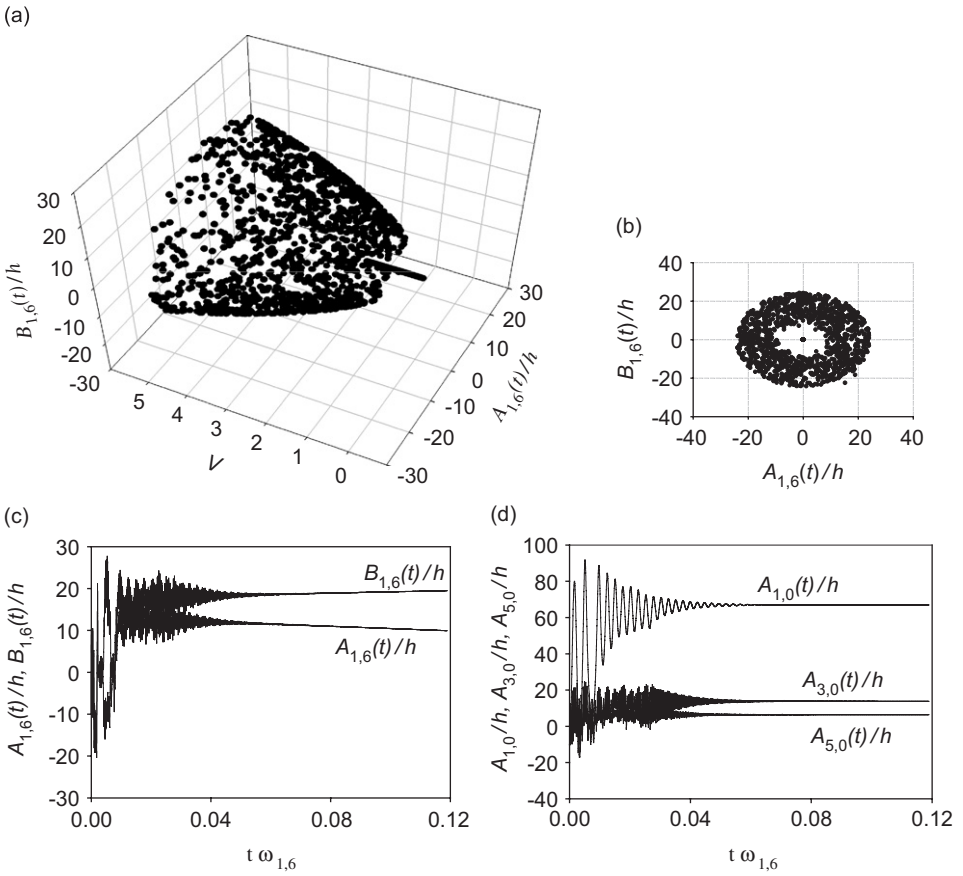

Fig. 8. Evolution of the system solution starting from different initial conditions: (a) steady-state system response of $A_{1,6}(t)/h$ and $B_{1,6}(t)/h$ versus V; (b) two-dimensional view of the spiral-type solution for the generalized coordinates of the first asymmetric mode; (c) time history of $A_{1,6}(t)/h$ and $B_{1,6}(t)/h$ for $V = 4.1$; (d) time history of $A_{1,0}(t)/h$, $A_{3,0}(t)/h$ and $A_{5,0}(t)/h$ for $V = 4.1$.

An output controller (MATSUSHITA LM 10) was used to convert the laser signal to a voltage output. In the water-flow experiments, the MICRO-EPSILON optoNCDT 1400-200 sensor that has an output of 0–5 V was employed; it has a static resolution of 40 μm and a dynamic resolution of 200 μm at 1 kHz. The controller model (DAYTRONIC 3263P) used with the second laser system offers the option of three frequency output ranges (5000, 10 000, and 20 000 Hz) to capture possible vibrations of the shell during the experiments. Both laser systems were calibrated and the voltage outputs were converted to shell amplitude in millimeters.

4.1. Annular air-flow experiments

4.1.1. General discussion of the experiments

Fig. 9 shows the apparatus used in the annular flow experiments. In the upper part, above the surface of the "table", an elastomer shell is clamped at both ends and positioned coaxially within an outer rigid plexiglas tube, which provides the outer containment of the annular flow. Specially designed supports provide the clamped boundary conditions for the elastomer shell, which is glued to thick, solid metal supports. In these experiments, the annular gap was set at 6.4 mm.

The lower part of the apparatus consists of an axisymmetric plenum chamber with contracting ends. Inside the chamber, the well-mixed air-stream, prior to entering the annular region, is further rendered uniform and straight by flowing through an annular region provided by a long solid cylinder with an ogival streamlined lower end. The annular passage, from its upstream end (i.e., from the ogival end of the "upstream cylinder", Fig. 9) to the upstream end of the shell, is approximately $50D_h$ long, where D_h is the hydraulic diameter; hence

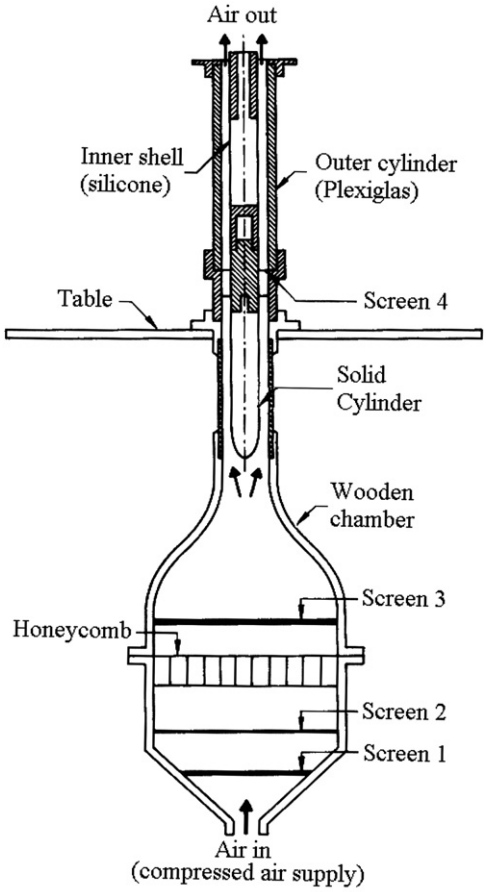

Fig. 9. Experimental apparatus for annular air-flow experiments with elastomer shells (after Ref. [7]).

the Reynolds number (based on the hydraulic diameter) at instability, is $Re_{D_h} \sim O(10^4)$, and the flow should be turbulent and fully developed. The air is supplied, at the bottom of the chamber, from a bank of compressors interconnected to a surge tank, providing air at about 690 kPa.

Additional experiments were conducted to assess the effect of a steady transmural pressure difference, $\Delta P_{tm}(x) = P_{\text{ann}}(x) - P_{\text{inn}}$, where $P_{\text{ann}}(x)$ is the static pressure in the annulus at a specific point, e.g. at the downstream end of the shell ($x = L$), and P_{inn} is the uniform static pressure of the quiescent inner fluid. Two typical types of such experiments were conducted. In one, $P_{\text{inn}} = P_a$ was imposed (P_a being the atmospheric pressure), by venting the inner space (within the shell) to atmosphere; this gives significant pressurization, increasing with flow. In the other type of experiments, $P_{\text{inn}} = P_{\text{ann}}(L)$ was imposed by providing an appropriate connection between the annulus at $x = L$ and the inner space; this gives a moderate triangular pressurization along the shell length, again increasing with flow. In both cases, the external pressure was larger than that within the shell. Details are given in Karagiozis [37].

The air-flow velocity was measured via orifice plates of appropriate size, located upstream of the apparatus, and calculated by standard methods [49].

4.1.2. Experimental results for clamped shells in annular air-flow

Karagiozis et al. [40] presented some earlier experiments with a clamped elastomer shell in annular flow. In all cases the shell lost stability by divergence. They also presented results that indicated that enhanced inwards intramural pressurization of the shell, i.e., larger inward-directed pressure difference across the shell wall, severely destabilizes the shell. This indeed is expected since it is clear that, if the pressurization were increased sufficiently, the shell would buckle (collapse inwards) even with no flow. In an investigation of the

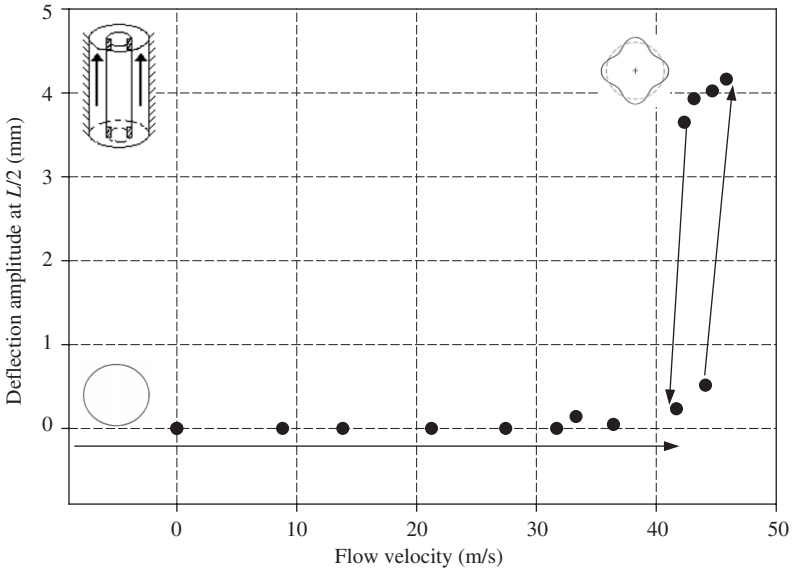

Fig. 10. Bifurcation diagram for a clamped elastomer shell in annular air-flow, for $L/R = 1.7$ and moderate intramural pressure $\Delta P_{tm} = P_{\text{ann}}(x) - P_{\text{inn}}$. The circumferential wavenumber was $n = 4$.

effect of length-to-radius ratio of the shell it was found that, as the length was reduced, the circumferential wavenumber associated with divergence increased, which accords with previously found results [2]. It was found that these observations agree qualitatively with linear and nonlinear theoretical predictions [8,34].

Fig. 10 shows some new experimental results in the form of a bifurcation diagram, as a plot of the dimensional shell deflection at mid-length of the shell versus the dimensional air-flow velocity U. In this case $\Delta P_{tm} = P_{\text{ann}}(x) - P_{\text{inn}} > 0$ with $P_{\text{inn}} = P_{\text{ann}}(L)$. At small U the shell remained stable, with small static deformations of about 0.5 mm as U reached values less than 45.85 m/s; this small shell axisymmetric deformation is related to the growth of the pressurization with flow. At $U = 45.85$ m/s the shell lost stability by divergence, reaching amplitudes of 4.2 mm at mid-length. This shell amplitude is 2.8 times the shell thickness, indicating a large deformation associated with the radial contraction of the shell wall. The divergence (buckling) was associated with a circumferential wavenumber (number of nodal diameters) of $n = 4$, which agrees with previous experimental results and theoretical calculations [5,40].

The flow velocity was then decreased slowly, and more data points were recorded, as shown in Fig. 10. At $U = 41.7$ m/s, the shell returned to its original circular shape and very small axisymmetric deformation. This flow-dependent hysteresis indicates that the divergence is subcritical; i.e., the nonlinear behaviour is of the softening type. This subcritical behaviour of the shell has been confirmed by repeating the experiment a number of times.

Additional experiments were conducted to study the effect of the intramural pressurization on the stability of the shell. In all experiments the shell lost stability by divergence, experiencing a strong hysteresis (subcritical nonlinear response).

Table 3 lists the critical flow velocity for divergence and the restabilization air-flow velocity observed for all sets of experiments.

4.2. Internal air-flow experiments

4.2.1. General description of the experiments

The internal air-flow apparatus is a variant of that shown in Fig. 9, adapted to channel the air from the plenum chamber to the elastomer shell, which is mounted in a very similar manner as for the annular flow experiments. The outer plexiglas tubular cylinder, providing the clamped supports to the shell, is located coaxially around the shell, with large enough annular gap for the annular fluid to have essentially no

Table 3
Summary of the experimental data for a clamped elastomer shell in annular air-flow

Experiment	L/R	ΔP_{tm} (Pa)	U_c (m/s)	U_R (m/s)	$w_{x=L/2}/h$
EA 1	1.7	$\Delta P_{tm} = P_{\text{ann}}(x) - P_{\text{inn}}(L)$	42.08	37.39	0.65
EA 2	1.7	$\Delta P_{tm} = P_{\text{ann}}(x) - P_{\text{inn}}(L)$	43.97	36.48	3.12
EA 3	1.7	$\Delta P_{tm} = P_{\text{ann}}(x) - P_{\text{a}}$	24.86	18.40	3.21
EA 4	1.7	$\Delta P_{tm} = P_{\text{ann}}(x) - P_{\text{inn}}(L)$	46.28	39.61	2.71
EA 5	1.7	$\Delta P_{tm} = P_{\text{ann}}(x) - P_{\text{inn}}(L)$	45.85	36.43	2.78
EA 6	1.7	$\Delta P_{tm} = P_{\text{ann}}(x) - P_{\text{a}}$	24.96	21.05	2.87
EA 7	1.7	$\Delta P_{tm} = P_{\text{ann}}(x) - P_{\text{inn}}(L)$	46.29	42.06	3.06
EA 8	1.7	$\Delta P_{tm} = P_{\text{ann}}(x) - P_{\text{inn}}(L)$	37.36	33.4	3.21
EA 9	1.7	$\Delta P_{tm} = P_{\text{ann}}(x) - P_{\text{inn}}(L)$	34.8	28.49	1.47
EA 10	1.7	$\Delta P_{tm} = P_{\text{ann}}(x) - P_{\text{inn}}(L)$	40.53	35.82	3.46
EA 11	1.7	$\Delta P_{tm} = P_{\text{ann}}(x) - P_{\text{a}}$	22.53	19.05	1.99

ΔP_{tm} is the intramural pressure; U_c is the critical flow velocity for buckling; U_R is the restabilization air-flow velocity; $w_{x=L/2}/h$ is the ratio of the shell amplitude over the thickness of the shell.

dynamical effect on the system. In some experiments, a thin aluminium rod was mounted at the centre of the elastomer shell to enable reaching higher flow velocities with the available air supply.

As in the annular experiments, different transmural pressure arrangements were possible, but in these experiments $P_{\text{ann}} = P_{\text{inn}} = (0)$ was imposed throughout; therefore a moderate triangular pressurization along the shell length, increasing with flow, was imposed, with the pressurization force acting inwards.

Measurement methods were the same as for annular flow. Further details, in this case also, may be found in Ref. [40].

4.2.2. Experimental results of clamped elastomer shells with internal air-flow

In all internal air-flow cases the shell system lost stability by divergence leading to oscillatory or "*dynamic*" divergence. The mechanism of dynamic divergence has been discussed in detail in Karagiozis et al. [40]; briefly, it is as follows: (i) the shell loses stability by static divergence; but, due to the large flexibility of the elastomer shell, the deformation is large enough (in many cases reducing the flow area by 50% or more), to cause a pressure build-up upstream of the shell; (ii) this pressure build-up causes the shell to open up and to buckle in the antiphase shape; (iii) this phenomenon is repeated again and again, giving the impression of an oscillatory instability. Fig. 11 shows in a series of photographs the dynamic buckling phenomenon, as observed for a shell with $L/R = 2$ and $n = 4$.

In Ref. [40] it was concluded that very pliable shells lose stability by divergence, giving rise to this dynamic buckling phenomenon, because of the large flow-constricting shell deformation involved. It is believed that Païdoussis and Denise [3] observed the same phenomenon in their experiments but misinterpreted it as flutter; see also Ref. [2].

4.3. Internal water-flow experiments

4.3.1. General discussion

The water-flow apparatus involves a modification of the vertical test-section of a water tunnel such that the flow from the upper part of a 203 mm diameter test-section is channelled into the test shell, which is of considerably smaller diameter, as shown in Fig. 12. The test shell is surrounded by quiescent water; the pressure in that fluid region was made higher than the pressure in the internally flowing fluid at mid-length of the shell, i.e., $P_{\text{ann}} > P_{\text{inn}}(L/2)$, as shown in the figure. Thus, there was a net inwards transmural pressure. This was necessary to achieve flow-induced instability for some of the shells, because of the limited maximum flow velocity available in the water tunnel.

Experiments were conducted with two types of shells, made from aluminium or PET plastic, glued to copper rings. The rings sat on plastic supports in the test-section and were sealed with silicone rubber. The results are presented in the following two subsections.

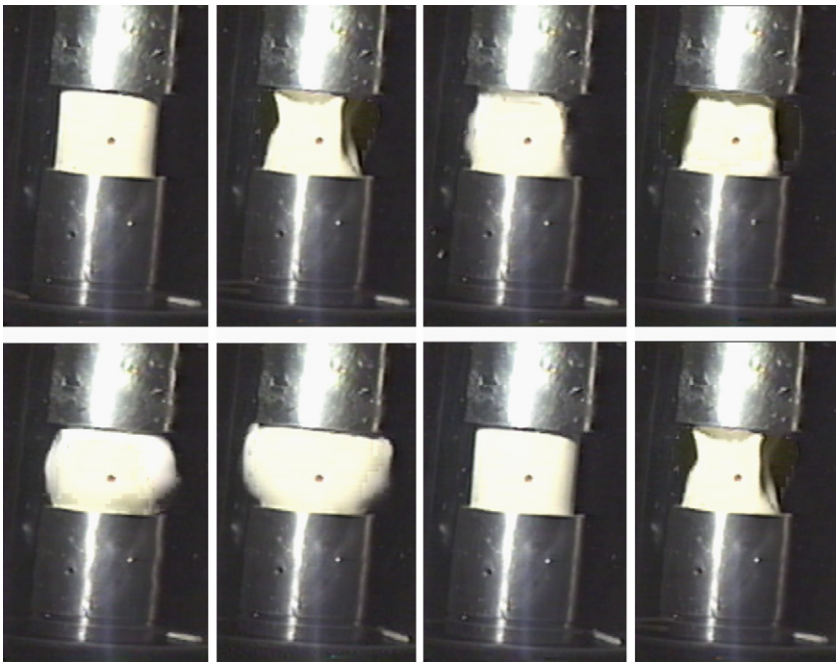

Fig. 11. Dynamic divergence video-sequence for a clamped elastomer shell subjected to internal air-flow for $L/R = 2$. The circumferential wavenumber was $n = 4$.

4.3.2. Experimental results of clamped aluminium shells with internal water flow

Two representative sets of results from these experiments are shown in Fig. 13. The transmural pressure was set at $\Delta P_{tm} = P_{\text{ann}} - P_{\text{inn}}(L/2) = 4.5$ and 5.7 kPa, respectively, and it was kept constant as the flow velocity was varied. In both experiments, the flow velocity was incremented until instability occurred. In the case of $\Delta P_{tm} = 4.5$ kPa, the shell lost stability by divergence at $U_c = 16.1$ m/s with a circumferential wavenumber of $n = 6$. The shell amplitude at the onset of buckling was 2.8 mm, about 20 times the shell thickness. When slowly decreasing the flow velocity, the shell amplitude also decreased until the original circular cross-sectional shape was restored at $U = 15.3$ m/s. In the second set of experiments with $\Delta P_{tm} = 5.7$ kPa the critical flow velocity for divergence was $U_c = 16.0$ m/s, also with $n = 6$.

In all experiments with aluminium shells, the shell lost stability by divergence, exhibiting a strong subcritical nonlinear response. In contrast to the elastomer shells, the flexural rigidity here is sufficiently large to result in a relatively small amplitude at divergence (compared to the shell radius), hence incurring no appreciable constriction of the flow area. This is believed to be the reason for the non-occurrence of dynamic divergence in this case.

4.3.3. Experimental results of clamped PET shells with internal water flow

The PET shells offer the advantage of a lower Young's modulus compared to aluminium shells, as shown in Table 2. In these experiments, the transmural pressure, $\Delta P_{tm} = P_{\text{ann}} - P_{\text{inn}}(L/2)$, was generally lower than in the aluminium shell experiments. In the two sets of experiments to be presented, ΔP_{tm} was set at 4.2 and 4.5 kPa, respectively.

The results are shown in Fig. 14 as a plot of shell deflection amplitude measured at $x = L/2$ versus flow velocity. In the case of $\Delta P_{tm} = 4.5$ kPa, the flow was increased until buckling occurred at $U = 15.1$ m/s with $n = 6$; at the onset of buckling, the shell amplitude was 4.6 mm, or 15 times the shell thickness. The flow was then reduced in steps, and the shell amplitude was recorded at each step, as shown in the figure. At $U = 13.8$ m/s the shell regained its original cross-sectional circular shape. The results show a subcritical form of divergence with considerable hysteresis.

The experiment with $\Delta P_{tm} = 4.2$ kPa showed that in this case also, the loss of stability was subcritical. Again, because the buckling amplitudes were not so severe as to the result in significant flow constriction, the divergence observed was static rather than dynamic.

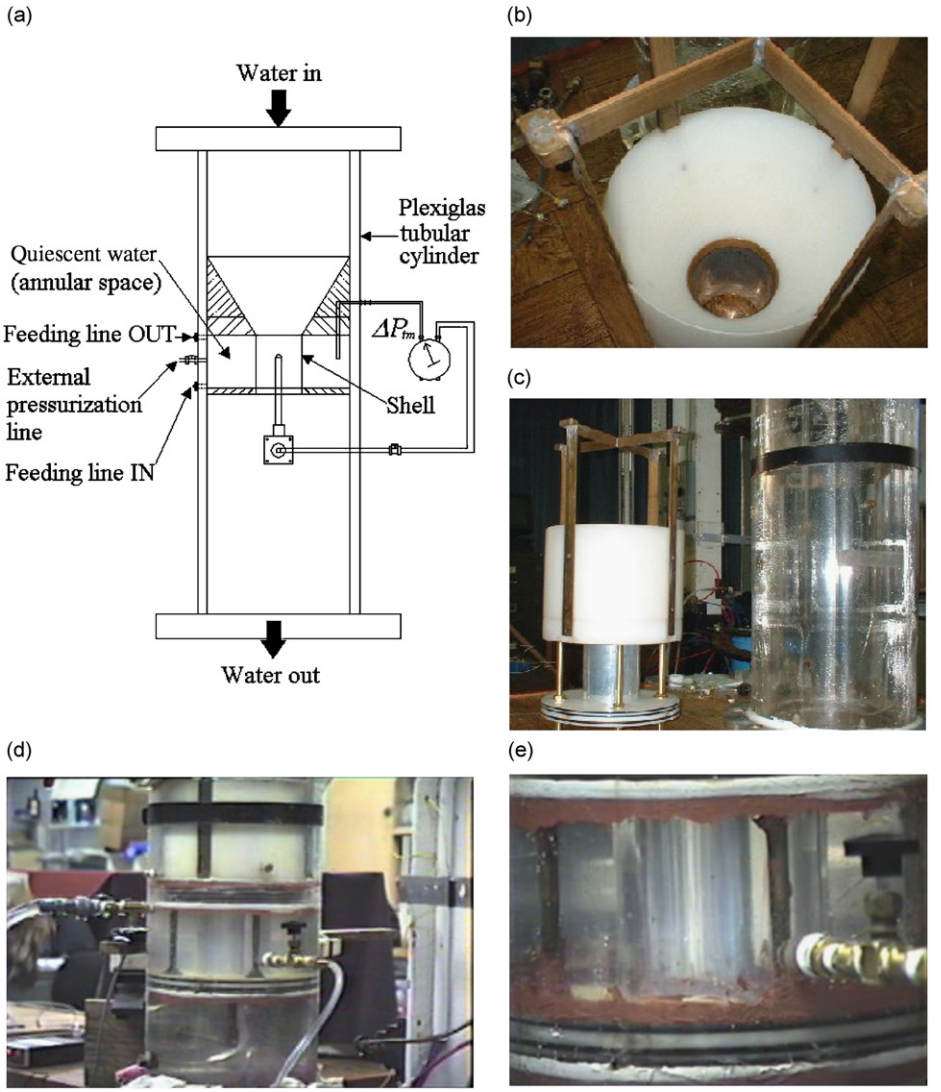

Fig. 12. View of the test-section of the water tunnel, with the apparatus for shells subjected to internal water flow mounted in it: (a) schematic of the test-section; (b) the plastic contraction, with the aluminium shell installed at its lower end; (c) the apparatus (left) before installation in the plexiglas test-section (right); (d) the test-section installed in the water tunnel; and (e) close-up of apparatus with an aluminium shell installed.

The two experiments in Fig. 14 were conducted with slightly different PET shells. It is to this that is attributed the fact that divergence for the shell with a higher ΔP_{tm} does not occur at a lower flow velocity than for the lower ΔP_{tm}.

5. Comparison of experimental and theoretical results

In this section, results obtained by the CC and SS theoretical nonlinear models are compared to the experimental results presented in Section 4 and some from Karagiozis et al. [40] for clamped elastomer, aluminium and PET shells subjected to annular or internal fluid flow.

It is well known [50], that in the presence of significant imperfections in the shell, rather inevitable in experiments, there is no interaction between the driven and companion modes, such as obtained in Fig. 8 of

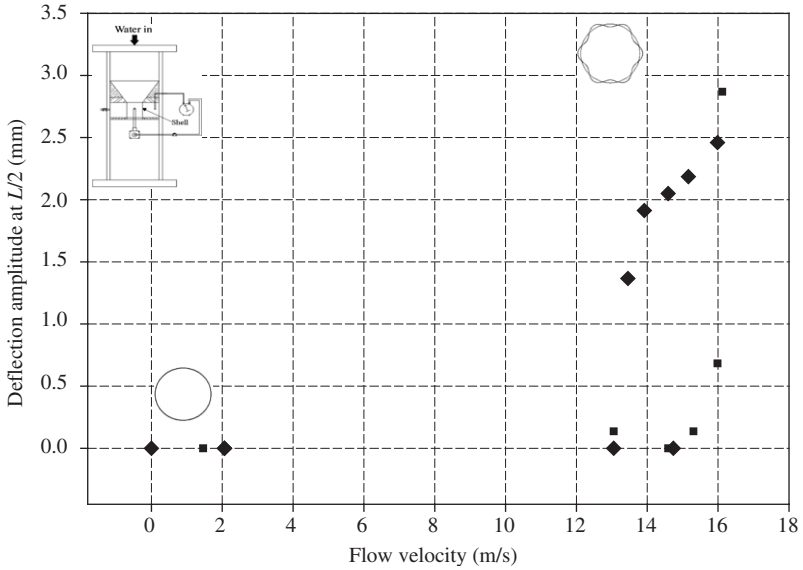

Fig. 13. Bifurcation diagram of an aluminium shell subjected to internal water flow with $n = 6$; ■, results with $P_{ann}-P_{inn}(L/2) = 4.5\,kPa$; ◆, results with $P_{ann}-P_{inn}(L/2) = 5.7\,kPa$.

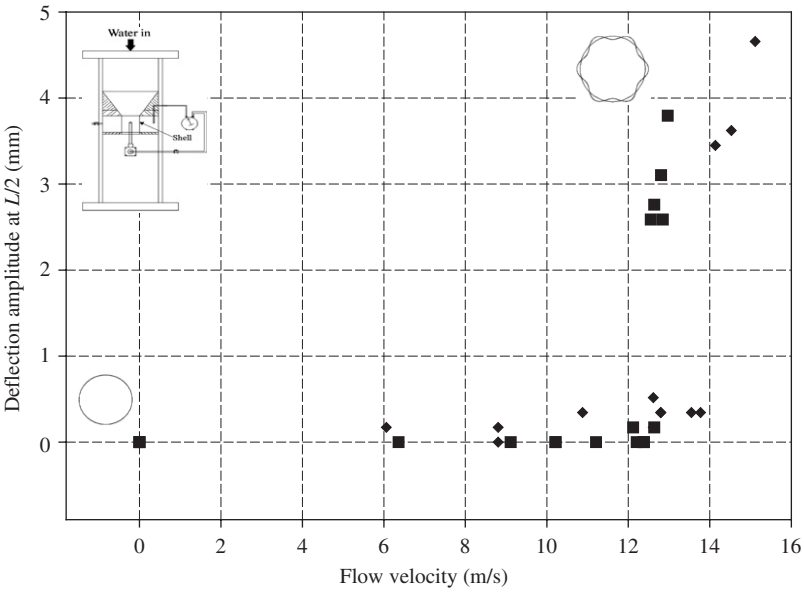

Fig. 14. Bifurcation diagram of PET shell subjected to internal water flow with $n = 6$: ◆, $P_{ann}-P_{inn}(L/2) = 4.5\,kPa$.; ■, $P_{ann}-P_{inn}(L/2) = 4.2\,kPa$.

the present study, for instance. Indeed, no helicoidal type of post-divergence behaviour was observed in any of the experiments. For this reason, in the theoretical calculations to be used for comparison with the experiments the companion mode has been ignored[4].

[4]It is interesting to retain the combination of companion and driven modes in the modal solution. In the case of a clamped elastomer shell with annular air-flow, a solution expansion involving driven and companion modes generates stable solutions predicting with greater accuracy some of the experimental results than when only the driven mode is assumed in the solution expansion. However, this kind of expansion cannot reproduce all the experimental data points. In the experiments, the spread in the results is related to initial shell imperfections, upstream and transmural pressure values and errors associated with the experimental procedure.

Experimental observations indicate that the maximum amplitude of the shell deformation occurred at or close to mid-length of the shell; therefore, all theoretical calculations of the shell amplitude were performed for $x = L/2$. In all cases the circumferential wavenumber value was set equal to the wavenumber observed in the experiments.

5.1. Elastomer shell in annular air-flow

A comparison of the theoretical results versus the experimental results obtained for the elastomer shell subjected to annular air-flow is shown in Fig. 15. This is a bifurcation diagram of the non-dimensional shell amplitude at $x = L/2$ versus the non-dimensional air-flow velocity, V. The theoretical results shown were obtained using two solution expansions: the seven and eight dof CC models. The eight dof model includes an additional axisymmetric mode in the solution expansion. The results of the eight dof model are so close to those obtained with the seven dof model as to be hardly distinguishable. In both cases the transmural pressure was set to $\Delta P_{tm}(L/2) = 0$ in this case, although in reality there is a small transmural pressure present in the experiments.

Both theoretical models predict that the linear onset of instability occurs at $V = 32.4$. The unstable solution Branch 2 generated at the bifurcation point becomes stable at $V = 23.7$. There is another stable Branch 2 that starts with negative amplitude values, indicating an outwards expansion of the shell wall, which eventually becomes positive because of the contribution of the axisymmetric modes to the total shell amplitude. As a consequence of all the experimental data having been measured on the shell at an angular position where the maximum inward displacement occurred, the larger positive Branch 2 must be used for comparison purposes.

The experimental data in Fig. 15 are from several experiments with the same system. As seen in the figure, some of the experimental results are close to the theoretical stable solution Branch 2. In fact, the experimental points that agree best with the theoretical results correspond to experiments in which the air-flow velocity was increased in very small increments up to the point of instability. However, regardless of the value of the air-flow increments, it was impossible to reach the linear threshold of $V = 32.4$ in the experiments, with the shell remaining stable.

These results indicate that the theoretical models predict with reasonably good accuracy the qualitative behaviour observed in the experiments. Both theoretical and experimental results indicate loss of stability by divergence, and no oscillatory motions in the velocity range considered. In addition, the theoretical results predict a large hysteresis between the onset of divergence and the folding point (the point at which unstable Branch 2 becomes stable), characterizing a subcritical post-buckling behaviour of the clamped elastomer shell; the same kind of hysteresis was also observed in the experiments.

However, in Fig. 15 some experimental points clearly do not lie close to the theoretical curves. Specifically, the experimental turning point is at rather lower flow velocity than the theoretical one. It was thought that, perhaps, the eight dof model was insufficiently accurate. Therefore, the eleven dof CC model was employed to generate a new bifurcation diagram. The eleven dof model includes four additional asymmetric modes

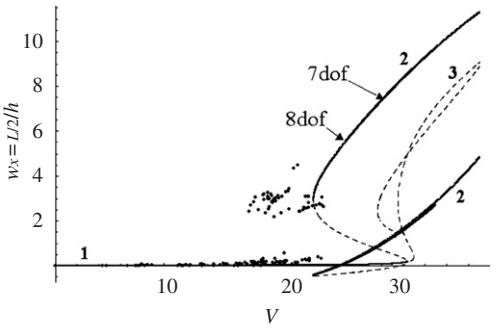

Fig. 15. Comparison of the experimental data obtained for an elastomer clamped shell subjected to annular air-flow and the results obtained by the seven and eight dof theoretical models (coincident to the naked eye): ————, stable solutions; – – – – –, unstable theoretical solutions; ●, experimental data points; 1, solution Branch 1; 2, solution Branch 2; 3, solution Branch 3.

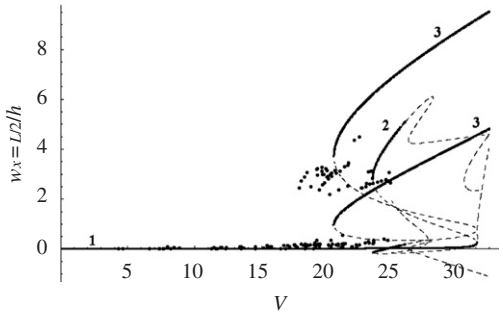

Fig. 16. Comparison of the experimental data obtained for an elastomer clamped shell subjected to annular air-flow and theoretical results obtained by the eleven dof theoretical model: ———, stable solutions; – – – – –, unstable theoretical solutions; ●, experimental data points.

(driven and companion) with $2n$ wavenumber. A comparison of the experimental points versus the theoretical results obtained with the eleven dof model is shown in Fig. 16.

The eleven dof model predicts loss of stability at $V = 31.1$, which is lower by 4% than that predicted in Fig. 15. At this flow velocity the stable solution of Branch 1 bifurcates to solution Branch 2. This solution branch folds at $V = 23.3$ and becomes stable (one solution line of Branch 2 is positive and the other crosses the zero amplitude axis). At a slightly different flow velocity, Branch 1 bifurcates to a different solution Branch 3. This solution folds at 20.4 and it also becomes a stable solution as shown in the figure.

The theoretical results shown in Fig. 16 are in excellent qualitative agreement and in fairly good quantitative agreement with the experimental observations (better than that achieved with the seven or eight dof models). In fact, these theoretical results can be used to explain the reason for the wide range of critical air-flow velocities observed in the experiments. There are at least three stable attracting solution branches, as shown in the figure. Therefore, for lower air-flow velocities, if enough perturbation is given to the system, for example in the form of a flow perturbation in the experiment, the system most probably will jump to the stable Branch 3. However, if the experiment is conducted with smaller air-flow velocity increments, thus eliminating or reducing sizable flow perturbations associated with stepping up the flow velocity, the solution could remain on stable Branch 1 until an inevitable perturbation causes a jump to either Branch 2 or 3, as shown in the figure. In the perfect case scenario, the experimental critical flow velocity should match the theoretical one of $V = 31.1$, but such ideal experimental conditions are clearly unattainable.

The fact that many experimental values for the threshold of divergence lie to the left of the theoretical curves may be attributed to the effect of imperfections and non-uniform pressure, not taken into account in the theoretical model.

A detailed discussion on the contribution of each mode in the mode expansion to the total theoretical solution for the results of Figs. 15 and 16 maybe found in Ref. [37].

5.2. Elastomer shell with internal air-flow

The theoretical nonlinear dynamics and stability of an elastomer clamped shell subjected to internal air-flow using the seven dof CC model was investigated extensively; the shell deformation was calculated at $x = L/2$ and $y = 0$. However, as mentioned in Section 4.2.2 the rather violent onset of dynamic divergence in the experiments did not permit gathering much useful experimental data for comparison with theory. In this section the theoretical results are compared to the single experimental point (for $L/R = 4.4$) reported in Karagiozis et al. [40]. This comparison is shown in Fig. 17.

The theoretically predicted large hysteretic nonlinear behaviour is validated by the experimental results. Quantitatively, the theoretical results are not in close enough agreement with the experimental point. It is suspected that this is mainly for two reasons. First, the experimental dynamic divergence was associated with $n = 3$, and hence so were the theoretical results; however, it is known that for $n < 4$ or 5 the Donnell shallow shell theory is strictly not valid, and therefore the theoretical results are not very reliable. Second, the

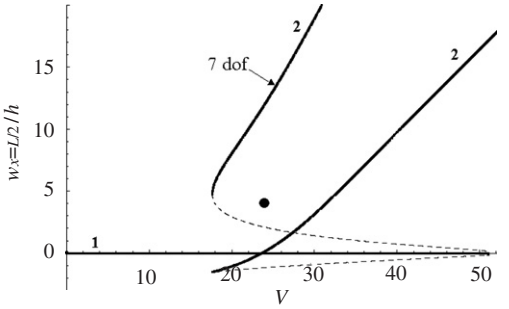

Fig. 17. Comparison of the experimental data point obtained for an elastomer clamped shell subjected to internal air-flow with $n = 3$ and theoretical results obtained by the seven degree-of-freedom theoretical model with $\Delta P_{tm}(L/2) = 0$ and $L/R = 4.4$ plotted in a bifurcation diagram of the non-dimensional shell amplitude versus the non-dimensional air-flow velocity; ————, stable solutions; – – – – –, unstable theoretical solutions; ●, experimental data point.

theoretical results are for static divergence, while the experimental ones for dynamic divergence. Specifically, the fluid–structure interaction model does not take into account the "upstream flow dynamics" which control the pressure variations associated with large deformations of the shell (the pressure build-up and release); thus, again, it cannot be expected that agreement between theory and experiment would be perfect.[5] Nevertheless, the experimental point is sufficiently close to the theoretical solution to lend support to the conclusion that the observed oscillation is indeed a dynamic divergence.

5.3. *Aluminium shell with internal water flow*

In this section the experimental results of an aluminium shell, clamped at both ends, conveying water are compared with the theoretical seven dof CC model. The density of the water was taken to be $\rho_F = 1000\,\mathrm{kg/m^3}$.

The comparison of the experimental and theoretical results is given in Fig. 18(a) in a non-dimensional bifurcation diagram of total shell deflection versus the dimensionless flow velocity at mid-length of the shell ($x = L/2$) for $\Delta P_{tm}(L/2) = 5.8\,\mathrm{kPa}$.

The theoretical results predict loss of stability by divergence at $V = 4.25$. The unstable Branch 2 becomes stable after folding at $V = 2.24$. All models predict a similar subcritical response for the shell, with large hysteresis. The solutions are all static, in the velocity range used in the numerical calculations. The theoretical results are in qualitative agreement with the experimental ones, but the quantitative agreement is poor. The main reason for the difference between the experimental and theoretical results may be attributed to the experimental boundary conditions, which were insufficiently "good" to provide the ideal clamping of the shell assumed in theory. This is obvious in the comparison between the theoretical and experimental in-air natural frequencies of the shell, specifically because in the experiments the "clamping" of the ends was not perfect by any means. This is clear in Table 4, where the experimental and theoretical values of the natural frequency for $m = 1$ and $n = 6$ of the aluminium shell in air are compared. The experimental frequency results were obtained with the shell supported at its two ends as in Fig. 12(a), using hammer excitation (B&K 8203) along with a Polytec laser Doppler vibrometer (OFV 5000 with laser head OFV 505) and the LMS CADA-X software for modal identification. The theoretical results listed are for simply supported and clamped boundary conditions using the Donnell nonlinear shallow-shell theory.

It is seen in Table 4 that the natural frequency of the experimental shell lies between the theoretical values for clamped and simply supported ends. In the flow and vibration experiments, the aluminium shell was glued to copper rings at both ends. The boundary conditions of the glued shell do not truly represent the clamped boundary conditions used by the theoretical model. Furthermore, the apparatus allowed for small axisymmetric motion at the interface of the shell with the bottom boundary surface of the plastic contraction

[5]For the same reason, and also because the observed oscillation was with $n = 2$, this theory cannot be compared to the experimental data of Païdoussis and Denise [3].

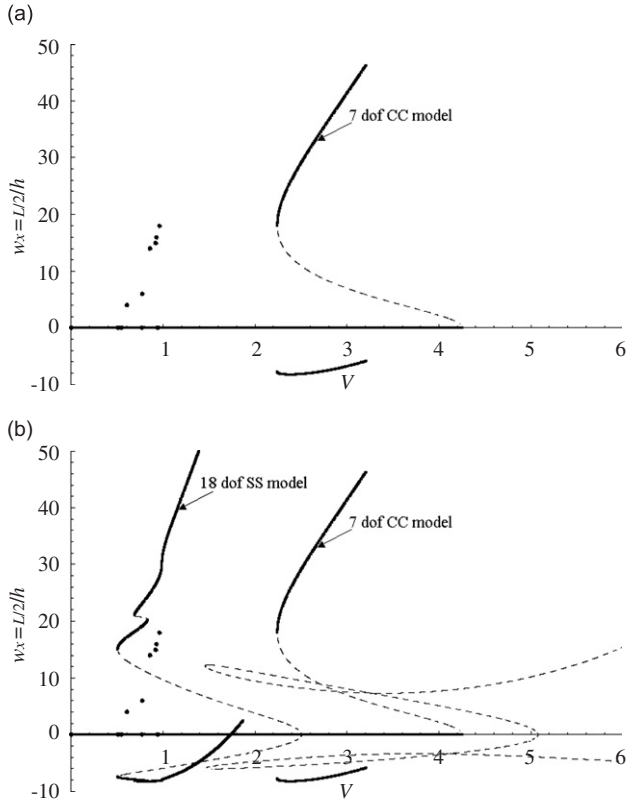

Fig. 18. Comparison of experimental data and theoretical results on a bifurcation diagram of the non-dimensional shell amplitude versus the non-dimensional water flow velocity at $x = L/2$ for an aluminium shell with internal water flow with $n = 6$ and transmural pressure of $\Delta P_{tm}(L/2) = 5.8\,\text{kPa}$; ————, stable solutions; – – – – –, unstable theoretical solutions; ●, experimental data points. (a) Seven dof model theoretical results with clamped–clamped boundary conditions and experimental results; (b) seven dof clamped–clamped model, 18 dof simply supported model and experimental results.

Table 4
Experimental and theoretical values of the natural frequency $\omega_{1,6}$ of a clamped and simply supported aluminium shell with the geometrical and material properties given beneath the table

Natural frequency	Theory-SS (Hz)	Experiment (Hz)	Theory-CC (Hz)
$\omega_{1,6}$	880	1261	1390

$L = 0.126\,\text{m}$; $R = 0.041125\,\text{m}$; $h = 0.000137\,\text{m}$; $\rho = 2850\,\text{kg/m}^3$; and $E = 66 \times 10^9\,\text{Pa}$; SS stands for simply supported and CC for clamped boundary conditions.

(Fig. 12), giving a boundary condition for axisymmetric modes with null axial force at the shell ends ($N_x = 0$). Therefore, it is expected that the experimental results would lie between the theoretical results for simply supported and clamped–clamped shells.

A comparison of the theoretical results for an aluminium shell with both ends simply supported (18 dof model) and clamped–clamped boundary conditions along with the experimental results is shown in Fig. 18(b). The results for the simply supported shell predict loss of stability with strong hysteresis also. It is clearly seen that the results of the simply supported shell are in excellent qualitative and closer quantitative agreement with the experimental results, but the amplitudes are overpredicted. Even the small jump in the experimental Branch 2 is predicted by the theoretical model. Quantitative differences can be attributed to the rotational constraint in the experimental model given by the glue and the ring, which is not included in the simply

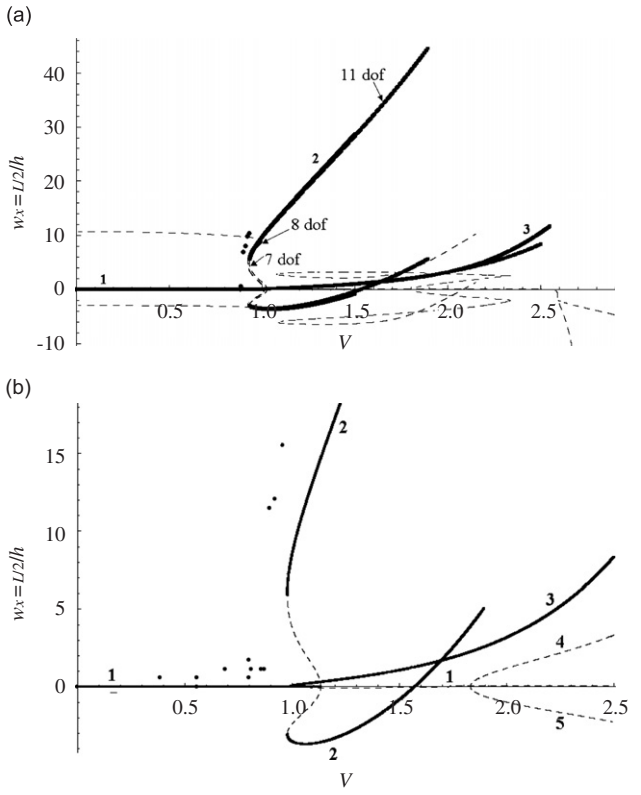

Fig. 19. Comparison of experimental data and theoretical results on a bifurcation diagram of the non-dimensional shell amplitude versus the non-dimensional water flow velocity at $x = L/2$ for a clamped PET shell with internal water flow and $n = 6$; ————, stable solutions; – – – – –·, unstable theoretical solutions; ●, experimental data points: (a) with a transmural pressure $\Delta P_{tm}(L/2) = 5.0\,\text{kPa}$; (b) with a transmural pressure of $\Delta P_{tm}(L/2) = 4.5\,\text{kPa}$.

supported model. Therefore, the experimental conditions in this case are closer to those of a simply supported shell than to a clamped shell; this is due to the fact that for a thin shell the axial constraint plays a much more significant role than the rotational constraint (the difference in moment, which in linear theory is the principal difference between clamped and simply supported ends).

Nevertheless, not too much should be made of the fact that the experimental results are so very near the theoretical ones for a simply supported shell; as it is known that imperfections cause the experimental points to migrate to the left (cf. discussion on Fig. 16), it is clear that in the absence of imperfections, the experimental results would be much closer to midway between the theoretical ones for a simply supported and a clamped shell.

5.4. Polyethylene terephthalate shell with internal water flow

The experimental results obtained for PET shell were used to validate the theoretical models of seven, eight and eleven dof. The boundary conditions of the PET shell are expected to be closer to clamped than achievable with the aluminium shells, simply because Young's modulus in this case is much lower.[6] The transmural pressure in this case was set to two different values: 5.0, 4.5 and 4.2 kPa. The comparison of the experimental and theoretical results for the total shell deformation, calculated at $x = L/2$, is shown in Fig. 19.

In the case of $\Delta P_{tm}(L/2) = 5.0\,\text{kPa}$, shown in Fig. 19(a), the theoretical seven dof model predicts loss of stability at a water-flow velocity of $V = 1.02$. The higher-order model (11 dof) reduces this critical flow velocity to $V = 1.00$. The unstable Branch 2 folds at a flow velocity of $V = 0.933$ (in the higher-order models

[6]Thus, the shell could deform appreciably without breaking the glue used at the clamped ends.

at $V = 0.927$) and becomes stable for higher flow velocities. The experimental results for $\Delta P_{tm}(L/2) = 5.0\,\text{kPa}$ are presented in Ref. [40]. In the case of $\Delta P_{tm}(L/2) = 4.5\,\text{kPa}$, shown in Fig. 19(b), a similar subcritical response with a hysteresis in returning to the original circular shape is observed for both experimental and theoretical results (obtained with the seven dof CC model). The quantitative agreement in this case is less good, but still quite good.

Generally for this case, the theoretical models are in excellent qualitative and good quantitative agreement with the experimental results. They predict loss of stability by divergence and a large hysteresis for the shell response. The velocity range under which the three models were investigated produced only static solutions for the shell response.

6. Conclusions

A theoretical nonlinear model has been developed in this paper for the dynamics of circular cylindrical shells containing or immersed in incompressible fluid flow, with both ends clamped. For the shell itself, the model utilizes the Donnell nonlinear shallow shell equations, while the fluid dynamics is modelled by linear potential flow theory.

Several versions of the theoretical model, referred to as different "models" in this paper, were constructed with differing modal composition for the shell deformation; namely, the seven, eight and eleven dof models (only the seven dof model being developed in detail in this paper, for brevity), plus an 18 dof model for simply supported shells.

Typical theoretical results are presented for shells with geometry and material properties corresponding to those used in the experiments, for both internal and annular flows. In all cases, it is found that the system loses stability, quite abruptly with increasing flow velocity, by static, strongly subcritical divergence. No post-divergence dynamic instabilities or other oscillatory solutions were found to exist.

The model found multiple stable solutions for specific values of the flow velocity, indicating that a jump from one stable solution to another is possible if enough perturbation is given to the shell system, as well as helicoidal solutions for imperfection-free systems; i.e., when both driven and companion modes are taken into account, it was found that, over a range of flow velocities, static deformation of the shell "travels" helicoidally around the shell surface as the flow velocity is increased.

Some hitherto unpublished experimental results are presented for (i) elastomer shells subjected to annular air-flow, (ii) elastomer shells with internal air-flow, (iii) aluminium shells with internal water flow, and (iv) PET shells with internal water flow.

In the experiments in (i), (iii) and (iv), it was found that the system lost stability by static divergence (buckling). Moreover, a strong hysteresis between the onset and, as the flow velocity was decreased, the cessation of divergence was found. Both these findings are in full qualitative agreement with the predictions of the theoretical model of a strongly subcritical static divergence. In the case of elastomer shells conveying air-flow, case (ii) of the previous paragraph, the shell was observed to lose stability dynamically with very large amplitudes. However, as reasoned in Païdoussis [6] and Karagiozis et al. [40] and by comparison with the behaviour in (iii) and (iv), it was concluded that what appears as an oscillatory instability is in fact a dynamic divergence phenomenon, associated with the flow constriction resulting from the large amplitudes of divergence in such pliable shells. Significantly, with the stiffer aluminium and PET shells, the system lost stability by static divergence, in agreement with the theoretical model.

In terms of quantitative agreement for the threshold of divergence and the post-divergence amplitudes, excellent agreement was obtained for the PET shells conveying water and the elastomer shells in annular air-flow, which thus suggests that the theoretical model is basically sound. In the case of aluminium shells conveying water, despite the excellent qualitative agreement between theory and experiment, the two sets of results were in poor quantitative agreement. However, it was found that the experimental results are in much better agreement with the model for simply supported ends; this is because of the axial flexibility of the constraints in the experiment, rendering the experimental supports closer to simple supports.

In the case of elastomer shells conveying air, agreement was not expected to be close, in view of the fact that theory predicts static divergence while in the experiments a dynamic one was observed, and for other reasons,

as discussed in Section 4.2. Nevertheless, the one experimental point that could be recorded was sufficiently close to the theoretical result, to lend further support to the validation of the theoretical model.

In all comparisons of theory with experiment, the theoretical calculations were conducted in the absence of companion mode participation, on the reasonable grounds that imperfections in the experimental system would destroy any possible coupling between the two. Thus, the helicoidal evolution of divergence with increasing flow velocity found in Section 3 was not possible in these theoretical results and, indeed, was never observed in the experiments, most probably because of imperfections.

In general, the theoretical models predicted with excellent accuracy the qualitative changes in shell behaviour, and with reasonably good or excellent quantitative agreement the critical and post-divergence behaviour of the experimental systems investigated. The model found multiple stable solutions for specific values of the flow velocity, indicating that a jump from one stable solution to another is possible if enough perturbation is given to the system.

From the design point of view, this study shows that the critical flow velocity for shells cannot be predicted by a linear analysis, and that existing safety criteria may be inadequate, due to the subcritical bifurcation associated with loss of stability, confirming the conclusions reached earlier by Amabili et al. [29].

Acknowledgements

The authors would like to thank NSERC of Canada and FQRNT of Québec for providing financial support for this research. This work was also partially supported by the Italy–Québec scientific and technological cooperation programme of the Italian Ministry of Foreign Affairs and the Québec Ministry of International Relations.

Appendix A. Additional expressions for Section 2

A.1. Equations of motion of the seven dof model

The remaining equations of motion, other than the first, for the seven dof model are given below

$$\begin{aligned}
&m_{2,n}\ddot{B}_{1,n}(t)+c_{2,n}\dot{B}_{1,n}(t)+k_{2,n}B_{1,n}(t)+\beta_1B_{1,n}(t)A_{1,0}(t)+\beta_2B_{1,n}(t)A_{1,0}^2(t)\\
&\quad+\beta_3A_{1,n}^2(t)B_{1,n}(t)+\beta_4A_{1,n}(t)A_{2,n}(t)B_{1,n}(t)+\beta_5B_{1,n}(t)A_{2,n}^2(t)+\beta_6B_{1,n}(t)A_{3,0}(t)\\
&\quad+\beta_7B_{1,n}(t)A_{1,0}(t)A_{3,0}(t)+\beta_8B_{1,n}(t)A_{3,0}^2(t)+\beta_9B_{1,n}(t)A_{5,0}(t)\\
&\quad+\beta_{10}B_{1,n}(t)A_{1,0}(t)A_{5,0}(t)+\beta_{11}B_{1,n}(t)A_{3,0}(t)A_{5,0}(t)+\beta_{12}B_{1,n}(t)A_{5,0}^2(t)\\
&\quad+\beta_{13}B_{1,n}^3(t)+\beta_{14}B_{2,n}(t)A_{1,n}^2(t)+\beta_{15}A_{1,n}(t)A_{2,1}(t)B_{2,n}(t)+\beta_{16}B_{2,n}(t)A_{2,n}^2(t)\\
&\quad+\beta_{17}B_{2,n}(t)A_{3,0}(t)+\beta_{18}A_{1,0}(t)A_{3,0}(t)B_{2,n}(t)+\beta_{19}B_{2,n}(t)A_{3,0}^2(t)\\
&\quad+\beta_{20}B_{2,n}(t)A_{5,0}(t)+\beta_{21}A_{1,0}(t)A_{5,0}(t)B_{2,n}(t)+\beta_{22}A_{3,0}(t)A_{5,0}(t)B_{2,n}(t)\\
&\quad+\beta_{23}B_{2,n}(t)A_{5,0}^2(t)+\beta_{24}B_{2,n}(t)B_{1,n}^2(t)+\beta_{25}B_{1,n}(t)B_{2,n}^2(t)+\beta_{26}B_{2,n}^3(t)=0,
\end{aligned}\tag{A.1}$$

$$\begin{aligned}
&m_{3,n}\ddot{A}_{2,n}(t)+c_{3,n}\dot{A}_{2,n}(t)+k_{3,n}A_{2,n}(t)+\gamma_1A_{1,n}^3(t)+\gamma_2A_{1,0}(t)A_{2,n}(t)\\
&\quad+\gamma_3A_{1,0}^2(t)A_{2,n}(t)+\gamma_4A_{2,n}(t)A_{1,n}^2(t)+\gamma_5A_{1,n}(t)A_{2,n}^2(t)+\gamma_6A_{2,n}^3(t)\\
&\quad+\gamma_7A_{1,n}(t)A_{3,0}(t)+\gamma_8A_{1,0}(t)A_{1,n}(t)A_{3,0}(t)+\gamma_9A_{2,n}(t)A_{3,0}(t)+\gamma_{10}A_{1,0}(t)A_{2,n}(t)A_{3,0}(t)\\
&\quad+\gamma_{11}A_{1,n}(t)A_{3,0}^2(t)+\gamma_{12}A_{2,n}(t)A_{3,0}^2(t)+\gamma_{13}A_{1,n}(t)A_{5,0}(t)+\gamma_{14}A_{1,n}(t)A_{1,0}(t)A_{5,0}(t)\\
&\quad+\gamma_{15}A_{2,n}(t)A_{5,0}(t)+\gamma_{16}A_{2,n}(t)A_{1,0}(t)A_{5,0}(t)+\gamma_{17}A_{1,n}(t)A_{3,0}(t)A_{5,0}(t)\\
&\quad+\gamma_{18}A_{2,n}(t)A_{3,0}(t)A_{5,0}(t)+\gamma_{19}A_{1,n}(t)A_{5,0}^2(t)+\gamma_{20}A_{2,n}(t)A_{5,0}^2(t)+\gamma_{21}A_{1,n}(t)B_{1,n}^2(t)\\
&\quad+\gamma_{22}A_{2,n}(t)B_{1,n}^2(t)+\gamma_{23}A_{1,n}(t)B_{1,n}(t)B_{2,n}(t)+\gamma_{24}A_{2,n}(t)B_{1,n}(t)B_{2,n}(t)\\
&\quad+\gamma_{25}A_{1,n}(t)B_{2,n}^2(t)+\gamma_{26}A_{2,n}(t)B_{2,n}^2(t)=0,
\end{aligned}\tag{A.2}$$

$$
\begin{aligned}
&m_{4,n}\ddot{B}_{2,n}(t)+c_{4,n}\dot{B}_{2,n}(t)+k_{4,n}B_{2,n}(t)+\delta_1A_{1,n}^2(t)B_{1,n}(t)+\delta_2B_{1,n}(t)A_{1,n}(t)A_{2,n}(t)\\
&\quad+\delta_3A_{2,n}^2(t)B_{1,n}(t)+\delta_4A_{1,0}(t)A_{3,0}(t)B_{1,n}(t)+\delta_5B_{1,n}(t)A_{3,0}^2(t)+\delta_6B_{1,n}(t)A_{5,0}(t)\\
&\quad+\delta_7B_{1,n}(t)A_{1,0}(t)A_{5,0}(t)+\delta_8B_{1,n}(t)A_{3,0}(t)A_{5,0}(t)+\delta_9B_{1,n}(t)A_{5,0}^2(t)\\
&\quad+\delta_{10}B_{1,n}^3+\delta_{11}B_{2,n}(t)A_{1,0}(t)+\delta_{12}B_{2,n}(t)A_{1,0}^2(t)+\delta_{13}A_{1,n}^2(t)B_{2,n}(t)\\
&\quad+\delta_{14}B_{2,n}(t)A_{2,n}(t)A_{1,n}(t)+\delta_{15}A_{2,n}^2(t)B_{2,n}(t)+\delta_{16}B_{2,n}(t)A_{3,0}(t)\\
&\quad+\delta_{17}B_{2,n}(t)A_{1,0}(t)A_{3,0}(t)+\delta_{18}A_{3,0}^2(t)B_{2,n}(t)+\delta_{19}B_{2,n}(t)A_{5,0}(t)\\
&\quad+\delta_{20}B_{2,n}(t)A_{5,0}(t)A_{1,0}(t)+\delta_{21}A_{3,0}(t)A_{5,0}(t)B_{2,n}(t)+\delta_{22}B_{2,n}(t)A_{5,0}^2(t)\\
&\quad+\delta_{23}B_{2,n}(t)B_{1,n}^2(t)+\delta_{24}B_{1,n}(t)B_{2,n}^2(t)+\delta_{25}B_{2,n}^3(t)=0,
\end{aligned}
\tag{A.3}
$$

$$
\begin{aligned}
&m_{1,0}\ddot{A}_{1,0}(t)+c_{1,0}\dot{A}_{1,0}(t)+k_{1,0}A_{1,0}(t)+\varepsilon_1A_{1,0}^2(t)+\varepsilon_2A_{1,0}^3(t)+\varepsilon_3A_{1,n}^2(t)\\
&\quad+\varepsilon_4A_{1,n}^2(t)A_{1,0}(t)+\varepsilon_5A_{1,n}(t)A_{2,n}(t)+\varepsilon_6A_{2,n}(t)A_{1,0}(t)A_{1,n}(t)\\
&\quad+\varepsilon_7A_{2,n}(t)A_{1,0}(t)A_{1,n}(t)+\varepsilon_8A_{2,n}^2(t)+\varepsilon_9A_{1,0}(t)A_{2,n}^2(t)+\varepsilon_{10}A_{1,0}(t)A_{3,0}(t)\\
&\quad+\varepsilon_{11}A_{1,0}^2(t)A_{3,0}(t)+\varepsilon_{12}A_{1,n}^2(t)A_{3,0}(t)+\varepsilon_{13}A_{1,n}(t)A_{2,n}(t)A_{3,0}(t)+\varepsilon_{14}A_{2,n}^2(t)A_{3,0}(t)\\
&\quad+\varepsilon_{15}A_{3,0}^2(t)+\varepsilon_{16}A_{1,0}(t)A_{3,0}^2(t)+\varepsilon_{17}A_{3,0}^3(t)+\varepsilon_{18}A_{5,0}(t)+\varepsilon_{19}A_{1,0}(t)A_{5,0}(t)\\
&\quad+\varepsilon_{20}A_{1,0}^2(t)A_{5,0}(t)+\varepsilon_{21}A_{1,n}^2(t)A_{5,0}(t)+\varepsilon_{22}A_{1,n}(t)A_{2,n}(t)A_{5,0}(t)\\
&\quad+\varepsilon_{23}A_{2,n}^2(t)A_{5,0}(t)+\varepsilon_{24}A_{3,0}(t)A_{5,0}(t)+\varepsilon_{25}A_{1,0}(t)A_{3,0}(t)A_{5,0}(t)\\
&\quad+\varepsilon_{26}A_{3,0}^2(t)A_{5,0}(t)+\varepsilon_{27}A_{5,0}^2(t)+\varepsilon_{28}A_{1,0}(t)A_{5,0}^2(t)+\varepsilon_{29}A_{3,0}(t)A_{5,0}^2(t)\\
&\quad+\varepsilon_{30}A_{5,0}^3(t)+\varepsilon_{31}B_{1,n}^2(t)+\varepsilon_{32}B_{1,n}^2(t)A_{1,0}(t)+\varepsilon_{33}A_{3,0}(t)B_{1,n}^2(t)+\varepsilon_{34}B_{1,n}^2(t)A_{5,0}(t)\\
&\quad+\varepsilon_{35}B_{2,n}(t)B_{1,n}(t)+\varepsilon_{36}B_{2,n}(t)A_{1,0}(t)B_{1,n}(t)+\varepsilon_{37}B_{2,n}(t)A_{3,0}(t)B_{1,n}(t)\\
&\quad+\varepsilon_{38}B_{2,n}(t)A_{5,0}(t)B_{1,n}(t)+\varepsilon_{39}B_{2,n}^2(t)+\varepsilon_{40}B_{2,n}^2(t)A_{1,0}(t)+\varepsilon_{41}B_{2,n}^2(t)A_{3,0}(t)\\
&\quad+\varepsilon_{42}B_{2,n}^2(t)A_{5,0}(t)=0,
\end{aligned}
\tag{A.4}
$$

$$
\begin{aligned}
&m_{3,0}\ddot{A}_{3,0}(t)+c_{3,0}\dot{A}_{3,0}(t)+k_{3,0}A_{3,0}(t)+\kappa_1A_{1,0}(t)+\kappa_2A_{1,0}^2(t)+\kappa_3A_{1,0}^3(t)\\
&\quad+\kappa_4A_{1,n}^2(t)A_{1,0}(t)+\kappa_5A_{1,n}(t)A_{2,n}(t)+\kappa_6A_{2,n}(t)A_{1,0}(t)A_{1,n}(t)\\
&\quad+\kappa_7A_{2,n}^2(t)+\kappa_8A_{1,n}^2(t)+\kappa_9A_{1,0}(t)A_{2,n}^2(t)+\kappa_{10}A_{1,0}(t)A_{3,0}(t)\\
&\quad+\kappa_{11}A_{1,0}^2(t)A_{3,0}(t)+\kappa_{12}A_{1,n}^2(t)A_{3,0}(t)+\kappa_{13}A_{1,n}(t)A_{2,n}(t)A_{3,0}(t)+\kappa_{14}A_{2,n}^2(t)A_{3,0}(t)\\
&\quad+\kappa_{15}A_{3,0}^2(t)+\kappa_{16}A_{1,0}(t)A_{3,0}^2(t)+\kappa_{17}A_{3,0}^3(t)+\kappa_{18}A_{5,0}(t)+\kappa_{19}A_{1,0}(t)A_{5,0}(t)\\
&\quad+\kappa_{20}A_{1,0}^2(t)A_{5,0}(t)+\kappa_{21}A_{1,n}^2(t)A_{5,0}(t)+\kappa_{22}A_{1,n}(t)A_{2,n}(t)A_{5,0}(t)\\
&\quad+\kappa_{23}A_{2,n}^2(t)A_{5,0}(t)+\kappa_{24}A_{3,0}(t)A_{5,0}(t)+\kappa_{25}A_{1,0}(t)A_{3,0}(t)A_{5,0}(t)\\
&\quad+\kappa_{26}A_{3,0}^2(t)A_{5,0}(t)+\kappa_{27}A_{5,0}^2(t)+\kappa_{28}A_{1,0}(t)A_{5,0}^2(t)+\kappa_{29}A_{3,0}(t)A_{5,0}^2(t)\\
&\quad+\kappa_{30}A_{5,0}^3(t)+\kappa_{31}B_{1,n}^2(t)+\kappa_{32}B_{1,n}^2(t)A_{1,0}(t)+\kappa_{33}A_{3,0}(t)B_{1,n}^2(t)+\kappa_{34}B_{1,n}^2(t)A_{5,0}(t)\\
&\quad+\kappa_{35}B_{2,n}(t)B_{1,n}(t)+\kappa_{36}B_{2,n}(t)A_{1,0}(t)B_{1,n}(t)+\kappa_{37}B_{2,n}(t)A_{3,0}(t)B_{1,n}(t)\\
&\quad+\kappa_{38}B_{2,n}(t)A_{5,0}(t)B_{1,n}(t)+\kappa_{39}B_{2,n}^2(t)+\kappa_{40}B_{2,n}^2(t)A_{1,0}(t)+\kappa_{41}B_{2,n}^2(t)A_{3,0}(t)\\
&\quad+\kappa_{42}B_{2,n}^2(t)A_{5,0}(t)=0,
\end{aligned}
\tag{A.5}
$$

$$
\begin{aligned}
&m_{5,0}\ddot{A}_{5,0}(t)+c_{5,0}\dot{A}_{5,0}(t)+k_{5,0}A_{5,0}(t)+\mu_1A_{1,0}(t)+\mu_2A_{1,0}^2(t)+\mu_3A_{1,0}^3(t)\\
&\quad+\mu_4A_{1,n}^2(t)A_{1,0}(t)+\mu_5A_{1,n}(t)A_{2,n}(t)+\mu_6A_{2,n}(t)A_{1,0}(t)A_{1,n}(t)\\
&\quad+\mu_7A_{2,n}^2(t)+\mu_8A_{1,n}^2(t)+\mu_9A_{1,0}(t)A_{2,n}^2(t)+\mu_{10}A_{1,0}(t)A_{3,0}(t)
\end{aligned}
$$

$$
\begin{aligned}
&+\mu_{11}A_{1,0}^2(t)A_{3,0}(t)+\mu_{12}A_{1,n}^2(t)A_{3,0}(t)+\mu_{13}A_{1,n}(t)A_{2,n}(t)A_{3,0}(t)+\mu_{14}A_{2,n}^2(t)A_{3,0}(t)\\
&+\mu_{15}A_{3,0}^2(t)+\mu_{16}A_{1,0}(t)A_{3,0}^2(t)+\mu_{17}A_{3,0}^3(t)+\mu_{18}A_{5,0}(t)+\mu_{19}A_{1,0}(t)A_{5,0}(t)\\
&+\mu_{20}A_{1,0}^2(t)A_{5,0}(t)+\mu_{21}A_{1,n}^2(t)A_{5,0}(t)+\mu_{22}A_{1,n}(t)A_{2,n}(t)A_{5,0}(t)\\
&+\mu_{23}A_{2,n}^2(t)A_{5,0}(t)+\mu_{24}A_{3,0}(t)A_{5,0}(t)+\mu_{25}A_{1,0}(t)A_{3,0}(t)A_{5,0}(t)\\
&+\mu_{26}A_{3,0}^2(t)A_{5,0}(t)+\mu_{27}A_{5,0}^2(t)+\mu_{28}A_{1,0}(t)A_{5,0}^2(t)+\mu_{29}A_{3,0}(t)A_{5,0}^2(t)\\
&+\mu_{30}A_{5,0}^3(t)+\mu_{31}B_{1,n}^2(t)+\mu_{32}B_{1,n}^2(t)A_{1,0}(t)+\mu_{33}A_{3,0}(t)B_{1,n}^2(t)+\mu_{34}B_{1,n}^2(t)A_{5,0}(t)\\
&+\mu_{35}B_{2,n}(t)B_{1,n}(t)+\mu_{36}B_{2,n}(t)A_{1,0}(t)B_{1,n}(t)+\mu_{37}B_{2,n}(t)A_{3,0}(t)B_{1,n}(t)\\
&+\mu_{38}B_{2,n}(t)A_{5,0}(t)B_{1,n}(t)+\mu_{39}B_{2,n}^2(t)+\mu_{40}B_{2,n}^2(t)A_{1,0}(t)+\mu_{41}B_{2,n}^2(t)A_{3,0}(t)\\
&+\mu_{42}B_{2,n}^2(t)A_{5,0}(t)=0,
\end{aligned}
\tag{A.6}
$$

where $m_{2,n}$, $m_{3,n}$, $m_{4,n}$, $m_{1,0}$, $m_{3,0}$ and $m_{5,0}$ are the corresponding modal mass coefficients after Galerkin projection; $c_{2,n}$ $c_{3,n}$, $c_{4,n}$, $c_{1,0}$, $c_{3,0}$ and $c_{5,0}$ the modal damping coefficients; $k_{2,n}$, $k_{3,n}$, $k_{4,n}$, $k_{1,0}$, $k_{3,0}$ and $k_{5,0}$ the modal stiffness coefficients; and $\beta_i(i=1,\ldots,26)$, $\gamma_i(i=1,\ldots,26)$, $\delta_i(i=1,\ldots,25)$, $\varepsilon_i(i=1,\ldots,42)$, $\kappa_i(i=1,\ldots,42)$ and $\mu_i(i=1,\ldots,42)$ are coefficients similar to the α_i in Eq. (48).

A.2. The perturbation pressure for the internal flow in the SS model

The expressions for $p_{\text{asymmetric}}^{\text{internal}}$ and $p_{\text{axisymmetric}}^{\text{internal}}$ for the simply supported shell are:

$$
\begin{aligned}
p_{\text{asymmetric}}^{\text{internal}}=\rho_F\times\Bigg[&\frac{\mathrm{I}_n(\pi R/L)2L(\ddot{A}_{1,n}(t)\cos(ny/R)+\ddot{B}_{1,n}(t)\sin(ny/R))}{(\mathrm{I}_{n-1}(\pi R/L)+\mathrm{I}_{n+1}(\pi R/L))\pi}\sin(\pi x/L)\\
&+\frac{\mathrm{I}_n(2\pi R/L)L(\ddot{A}_{2,n}(t)\cos(ny/R)+\ddot{B}_{2,n}(t)\sin(ny/R))}{(\mathrm{I}_{n-1}(2\pi R/L)+\mathrm{I}_{n+1}(2\pi R/L))\pi}\sin(2\pi x/L)\\
&+\frac{\mathrm{I}_n(\pi R/L)4\left(\dot{A}_{1,n}(t)\cos(ny/R)+\dot{B}_{1,n}(t)\sin(ny/R)\right)}{\left(\mathrm{I}_{n-1}(\pi R/L)+\mathrm{I}_{n+1}(\pi R/L)\right)}\cos(\pi x/L)\\
&+\frac{\mathrm{I}_n(2\pi R/L)4\left(\dot{A}_{2,n}(t)\cos(ny/R)+\dot{B}_{2,n}(t)\sin(ny/R)\right)}{\left(\mathrm{I}_{n-1}(2\pi R/L)+\mathrm{I}_{n+1}(2\pi R/L)\right)}\cos(2\pi x/L)\\
&-\frac{\mathrm{I}_n(\pi R/L)2\pi U^2\left(A_{1,n}(t)\cos(ny/R)+B_{1,n}(t)\sin(ny/R)\right)}{L(\mathrm{I}_{n-1}(\pi R/L)+\mathrm{I}_{n+1}(\pi R/L))}\sin(\pi x/L)\\
&-\frac{\mathrm{I}_n(2\pi R/L)4\pi U^2\left(A_{2,n}(t)\cos(ny/R)+B_{2,n}(t)\sin(ny/R)\right)}{L\left(\mathrm{I}_{n-1}(2\pi R/L)+\mathrm{I}_{n+1}(2\pi R/L)\right)}\sin\left(2\pi x/L\right)\Bigg]
\end{aligned}
\tag{A.7}
$$

and

$$
\begin{aligned}
p_{\text{axisymmetric}}^{\text{internal}}=\rho_F\times\Bigg[&\frac{\mathrm{I}_0(\pi R/L)L\ddot{A}_{1,0}(t)}{\mathrm{I}_1(\pi R/L)\pi}\sin(\pi x/L)+\frac{\mathrm{I}_0(3\pi R/L)L\ddot{A}_{3,0}(t)}{\mathrm{I}_1(3\pi R/L)3\pi}\sin(3\pi x/L)\\
&+\frac{\mathrm{I}_0(5\pi R/L)L\ddot{A}_{5,0}(t)}{\mathrm{I}_1(5\pi R/L)5\pi}\sin(5\pi x/L)+\frac{\mathrm{I}_0(\pi R/L)2U\dot{A}_{1,0}(t)}{\mathrm{I}_1(\pi R/L)}\cos(\pi x/L)\\
&+\frac{\mathrm{I}_0(3\pi R/L)2U\dot{A}_{3,0}(t)}{\mathrm{I}_1(3\pi R/L)}\cos(3\pi x/L)+\frac{\mathrm{I}_0(5\pi R/L)2U\dot{A}_{5,0}(t)}{\mathrm{I}_1(5\pi R/L)}\cos(5\pi x/L)\\
&-\frac{\mathrm{I}_0(\pi R/L)\pi U^2\dot{A}_{1,0}(t)}{\mathrm{I}_1(\pi R/L)L}\sin(\pi x/L)-\frac{\mathrm{I}_0(3\pi R/L)3\pi U^2\dot{A}_{3,0}(t)}{\mathrm{I}_1(3\pi R/L)L}\sin(3\pi x/L)\\
&-\frac{\mathrm{I}_0(5\pi R/L)5\pi U^2\dot{A}_{5,0}(t)}{\mathrm{I}_1(5\pi R/L)L}\sin(5\pi x/L)\Bigg].
\end{aligned}
\tag{A.8}
$$

A.3. The perturbation pressure for annular flow in the CC model

In the case of the CC seven dof model the perturbation terms are given by

$$\begin{aligned} p^{\text{annular}}_{\text{asymmetric}} = \sum_{m=1}^{MM} \rho_F (2L/m\pi) \left(\alpha^{\text{annular}}_{\text{asymmetric}} / \beta^{\text{annular}}_{\text{asymmetric}} \right) \\ \times \left[(\ddot{A}_{1,n}(t)\cos(ny/R) + \ddot{B}_{1,n}(t)\sin(ny/R))\psi_1 \sin(m\pi x/L) \right. \\ + (\ddot{A}_{2,n}(t)\cos(ny/R) + \ddot{B}_{2,n}(t)\sin(ny/R))\psi_2 \sin(m\pi x/L) \\ + (\dot{A}_{1,n}(t)\cos(ny/R) + \dot{B}_{1,n}(t)\sin(ny/R))\psi_1 (2Um\pi/L)\cos(m\pi x/L) \\ + (\dot{A}_{2,n}(t)\cos(ny/R) + \dot{B}_{2,n}(t)\sin(ny/R))\psi_2 (2Um\pi/L)\cos(m\pi x/L) \\ - (A_{1,n}(t)\cos(ny/R) + B_{1,n}(t)\sin(ny/R)) U^2 (m\pi/L)^2 \sin(m\pi x/L) \\ \left. -(A_{2,n}(t)\cos(ny/R) + B_{2,n}(t)\sin(ny/R)) U^2 (m\pi/L)^2 \sin(m\pi x/L) \right], \end{aligned} \tag{A.9}$$

where

$$\begin{aligned} \alpha^{\text{annular}}_{\text{asymmetric}} = \mathrm{K}_{n-1}(m\pi r_i/L)\mathrm{I}_n(m\pi R_o/L) + \mathrm{K}_{n+1}(m\pi r_i/L)\mathrm{I}_n(m\pi R_o/L) \\ + \mathrm{I}_{n+1}(m\pi r_i/L)\mathrm{K}_n(m\pi R_o/L) + \mathrm{I}_{n-1}(m\pi r_i/L)\mathrm{K}_n(m\pi R_o/L) \end{aligned} \tag{A.10}$$

and

$$\begin{aligned} \beta^{\text{annular}}_{\text{asymmetric}} = \mathrm{K}_{n-1}(j\pi r_i/L)\mathrm{I}_{n-1}(j\pi R_o/L) + \mathrm{K}_{n-1}(j\pi r_i/L)\mathrm{I}_{n+1}(j\pi R_o/L) \\ + \mathrm{K}_{n+1}(j\pi r_i/L)\mathrm{I}_{n-1}(j\pi R_o/L) + \mathrm{K}_{n+1}(j\pi r_i/L)\mathrm{I}_{n+1}(j\pi R_o/L) \\ - \mathrm{I}_{n+1}(j\pi r_i/L)\mathrm{K}_{n-1}(j\pi R_o/L) - \mathrm{I}_{n+1}(j\pi r_i/L)\mathrm{K}_{n+1}(j\pi R_o/L) \\ - \mathrm{I}_{n-1}(j\pi r_i/L)\mathrm{K}_{n-1}(j\pi R_o/L) - \mathrm{I}_{n-1}(j\pi r_i/L)\mathrm{K}_{n+1}(j\pi R_o/L). \end{aligned} \tag{A.11}$$

The contribution of the axisymmetric modes to the perturbation pressure is

$$\begin{aligned} p^{\text{annular}}_{\text{axisymmetric}} = \sum_{m=1}^{MM} \rho_F (L/m\pi) \frac{\left[\mathrm{K}_1(j\pi r_i/L)\mathrm{I}_0(j\pi R_o/L) + \mathrm{K}_0(j\pi R_o/L)\mathrm{I}_1(j\pi r_i/L) \right]}{\left[\mathrm{K}_1(j\pi r_i/L)\mathrm{I}_1(j\pi R_o/L) - \mathrm{I}_1(j\pi r_i/L)\mathrm{K}_1(j\pi R_o/L) \right]} \\ \times \left[(\ddot{A}_{1,0}(t)\psi_1 + \ddot{A}_{3,0}(t)\psi_3 + \ddot{A}_{5,0}(t)\psi_5) \sin(m\pi x/L) \right. \\ + (\dot{A}_{1,0}(t)\psi_1 + \dot{A}_{3,0}(t)\psi_3 + \dot{A}_{5,0}(t)\psi_5)(2Um\pi/L)\cos(m\pi x/L) \\ \left. -(A_{1,0}(t)\psi_1 + A_{3,0}(t)\psi_3 + A_{5,0}(t)\psi_5) U^2 (m\pi/L)^2 \sin(m\pi x/L) \right]. \end{aligned} \tag{A.12}$$

References

[1] E.H. Dowell, *Aeroelasticity of Plates and Shells*, Noordhoff International, Leyden, 1975.

[2] M.P. Païdoussis, *Fluid–Structure Interactions: Slender Structures and Axial Flow*, Vol. 2, Elsevier Academic Press, London, UK, 2003.

[3] M.P. Païdoussis, J.P. Denise, Flutter of thin cylindrical shells conveying fluid, *Journal of Sound and Vibration* 20 (1972) 9–26.

[4] G.T.S. Done, A. Simpson, Dynamic stability of certain conservative and non-conservative systems, *Institution of Mechanical Engineers—Journal of Mechanical Engineering Science* 19 (1977) 251–263.

[5] A. El Chebair, M.P. Païdoussis, A.K. Misra, Experimental study of annular-flow-induced instabilities of cylindrical shell, *Journal of Fluids and Structures* 3 (1989) 349–364.

[6] M.P. Païdoussis, Some unresolved issues in fluid–structure interactions, *Journal of Fluids and Structures* 20 (2005) 874–890.

[7] M.P. Païdoussis, *Fluid–Structure Interaction: Slender Structures and Axial Flow*, Vol. 1, Academic Press, London, 1998.

[8] M.P. Païdoussis, Some quandaries and paradoxes in fluid–structure interactions with axial flow, *Proceedings IUTAM Symposium on Fluid–Structure Interaction*, New Brunswick, NJ, USA, 2003, pp. 247–266.

[9] D.S. Weaver, T.E. Unny, On the dynamic stability of fluid-conveying pipes, *Journal of Applied Mechanics* 40 (1973) 48–52.

[10] D.S. Weaver, B. Myklatun, On the stability of thin pipes with an internal flow, *Journal of Sound and Vibration* 31 (1973) 399–410.

[11] L.K. Shayo, C.H. Ellen, The stability of finite length circular cross-section pipes conveying inviscid fluid, *Journal of Sound and Vibration* 37 (1974) 535–545.
[12] M.P. Païdoussis, S.P. Chan, A.K. Misra, Dynamics and stability of coaxial cylindrical shells containing flowing fluid, *Journal of Sound and Vibration* 97 (1984) 201–235.
[13] M.P. Païdoussis, A.K. Misra, S.P. Chan, Dynamics and stability of coaxial cylindrical shells conveying viscous fluid, *Journal of Applied Mechanics* 52 (1985) 389–396.
[14] A. El Chebair, A.K. Misra, M.P. Païdoussis, Theoretical study of unsteady viscous forces on inner- and annular-flow-induced instabilities of cylindrical shells, *Journal of Sound and Vibration* 138 (1990) 457–478.
[15] M.P. Païdoussis, V.B. Nguyen, A.K. Misra, A theoretical study of the stability of cantilevered coaxial cylindrical shells conveying fluid, *Journal of Fluids and Structures* 5 (1991) 127–164.
[16] V.B. Nguyen, M.P. Païdoussis, A.K. Misra, An experimental study of the stability of cantilevered coaxial cylindrical shells conveying fluid, *Journal of Fluids and Structures* 7 (1993) 913–930.
[17] V.B. Nguyen, M.P. Païdoussis, A.K. Misra, A CFD-based model for the study of the stability of cantilevered coaxial cylindrical shells conveying viscous fluid, *Journal of Sound and Vibration* 176 (1994) 105–125.
[18] R.O. Stearman, M.H. Lock, Y.C. Fung, Ames test on the flutter of cylindrical shells, Graduate Aeronautical Labs, California Institute of Technology, GALCIT Structural Dynamic Report SM 62–37, 1962.
[19] M.D. Olson, Y.C. Fung, Comparing theory and experiments for the supersonic flutter of circular cylindrical shells, *AIAA Journal* 5 (1967) 1849–1856.
[20] D.A. Evensen, M.D. Olson, Nonlinear flutter of a circular cylindrical shell in supersonic flow, NASA TN D-4265, 1967.
[21] G.W. Barr, R.O. Stearman, Influence of a supersonic flow-field on the elastic stability of cylindrical shells, *AIAA Journal* 8 (1970) 993–1000.
[22] W. Horn, G.W. Barr, L. Carter, R.O. Stearman, Recent contributions to experiments on cylindrical shell panel flutter, *AIAA Journal* 12 (1974) 1481–1490.
[23] L. Librescu, *Elastostatics and Kinetics of Anisotropic and Heterogeneous Shell-type Structures*, Noordhoff, Leiden, 1975.
[24] A.S. Vol'mir, *Shells in Flow of Liquid and Gas: Problems of Hydroelasticity*, Academy of Sciences (Nauka), Moscow, 1976 (in Russian).
[25] A.S. Vol'mir, *Shells in Flow of Gas and Liquid: Problems of Hydroelasticity*, Academy of Sciences (Nauka), Moscow, 1979 (in Russian).
[26] C. Guernier, Vibrations induced by flow in thin shells, Unpublished Report, Department of Mechanical Engineering, McGill University, 1978.
[27] A.A. Lakis, A. Laveau, Non-linear dynamic analysis of anisotropic cylindrical shells containing a flowing fluid, *International Journal of Solids and Structures* 28 (1991) 1079–1094.
[28] A. Selmane, A.A. Lakis, Non-linear dynamic analysis of orthotropic open cylindrical shells subjected to a flowing fluid, *Journal of Sound and Vibration* 202 (1997) 67–93.
[29] M. Amabili, F. Pellicano, M.P. Païdoussis, Nonlinear dynamics and stability of circular cylindrical shells containing flowing fluid. Part I: Stability, *Journal of Sound and Vibration* 225 (1999) 655–699.
[30] M. Amabili, F. Pellicano, M.P. Païdoussis, Non-linear dynamics and stability of circular cylindrical shells containing flowing fluid, Part II: large-amplitude vibrations without flow, *Journal of Sound and Vibration* 228 (1999) 1103–1124.
[31] M. Amabili, F. Pellicano, M.P. Païdoussis, Non-linear dynamics and stability of circular cylindrical shells containing flowing fluid, part III: truncation effect without flow and experiments,, *Journal of Sound and Vibration* 237 (2000) 617–640.
[32] M. Amabili, F. Pellicano, M.P. Païdoussis, Non-linear dynamics and stability of circular cylindrical shells containing flowing fluid, part IV: large-amplitude vibrations with flow, *Journal of Sound and Vibration* 237 (2000) 641–666.
[33] M. Amabili, F. Pellicano, M.P. Païdoussis, Non-linear dynamics and stability of circular cylindrical shells conveying flowing fluid, *Computers and Structures* 80 (2002) 899–906.
[34] M. Amabili, F. Pellicano, M.P. Païdoussis, Nonlinear stability of circular cylindrical shells in annular and unbounded axial flow, *Journal of Applied Mechanics* 68 (2001) 827–834.
[35] M. Amabili, F. Pellicano, Nonlinear supersonic flutter of circular cylindrical shells, *AIAA Journal* 39 (2001) 564–573.
[36] M. Amabili, F. Pellicano, Multimode approach to nonlinear supersonic flutter of imperfect circular cylindrical shells, *Journal of Applied Mechanics* 69 (2002) 117–126.
[37] K.N. Karagiozis, Experiments and Theory on the Nonlinear Dynamics and Stability of Clamped Shells Subjected to Axial Fluid Flow or Harmonic Excitation, PhD Thesis, McGill University, 2006.
[38] K.N. Karagiozis, M.P. Païdoussis, E. Grinevich, A.K. Misra, M. Amabili, Stability and non-linear dynamics of clamped circular cylindrical shells in contact with flowing fluid, *Proceedings IUTAM Symposium on Integrated Modeling of Fully Coupled Fluid–Structure Interactions*, Kluwer, Dordrecht, 2003, pp. 375–390.
[39] K.N. Karagiozis, M.P. Païdoussis, E. Grinevich, A.K. Misra, M. Amabili, Non-linear dynamics of clamped cylindrical shells subjected to flow, in: E. de Langre, F. Axisa (Eds.), *Proceedings Eighth International Conference on Flow-Induced Vibration*, Vol. I, Ecole Polytechnique, Paris, 2004, pp. 125–130.
[40] K.N. Karagiozis, M.P. Païdoussis, A.K. Misra, E. Grinevich, An experimental study of the nonlinear dynamics of cylindrical shells with clamped ends subjected to axial flow, *Journal of Fluids and Structures* 20 (2005) 801–816.
[41] K.N. Karagiozis, M. Amabili, M.P. Païdoussis, A.K. Misra, Nonlinear vibrations of fluid-filled clamped circular cylindrical shells, *Journal of Fluids and Structures* 21 (2005) 579–595.
[42] L.H. Donnell, *Beams, Plates and Shells*, McGraw-Hill, New York, 1976.

[43] Y. Matsuzaki, S. Kobayashi, A theoretical and experimental study of the nonlinear flexural vibration of thin circular cylindrical shells with clamped ends, *Transactions of the Japan Society for Aeronautical and Space Sciences* 12 (1969) 55–62.
[44] N. Yamaki, *Elastic Stability of Circular Cylindrical Shells*, North-Holland, Amsterdam, 1984.
[45] M. Amabili, Nonlinear vibrations of circular cylindrical shells with different boundary conditions, *AIAA Journal* 41 (2003) 1119–1130.
[46] P.B. Gonçalves, R.C. Batista, Non-linear vibration analysis of fluid-filled cylindrical shells, *Journal of Sound and Vibration* 127 (1988) 133–143.
[47] S. Wolfram, *The Mathematica Book*, fourth ed., Cambridge University Press, Cambridge, 1999.
[48] E.J. Doedel, A.R. Champneys, T.F. Fairgrieve, Y.A. Kuznetsov, B. Sandstede, X. Wang, *AUTO 97: Continuation and Bifurcation Software for Ordinary Differential Equations (with HomCont)*, Concordia University, Montreal, Canada, 1998.
[49] H.S. Bean, *Fluid Meters—Their Theory and Applications*, sixth ed., ASME, New York, 1971.
[50] M. Amabili, Theory and experiments for large-amplitude vibrations of empty and fluid-filled circular cylindrical shells with imperfections, *Journal of Sound and Vibration* 262 (2003) 921–975.